Experimental study of high energy muons from Extensive Air Showers in the energy range 100 TeV to 10 PeV

Henric George Sacha Wilkens

19th May 2003

Experimental study of high energy muons from Extensive Air Showers in the energy range 100 TeV to 10 PeV

Een wetenschappelijke proeve op het gebied
van Natuurwetenschappen, Wiskunde, en Informatica.

Proefschrift

ter verkrijging van de graad van doctor
aan de Katholieke Universiteit Nijmegen,
op gezag van de Rector Magnificus
prof. dr. C. W. P. M. Blom,
volgens besluit van het College van Decanen
in het openbaar te verdedigen
op woensdag 2 juli 2003,
des namiddags om 1:30 uur precies
door

Henric George Sacha Wilkens

geboren op 12 juni 1973 te Crest (Frankrijk)

Promotores:	**Prof. Dr. M. Pohl**	
	Prof. Dr. J. Kuijpers	
Copromotor:	**Dr. C. Timmermans**	
Manuscriptcommissie:	**Prof. Dr. K. Eggert**	CERN
	Dr. A. Haungs	Institut für Kernphysik Karlsruhe
	Prof. Dr. M. T. Dova	Universidad de La Plata
	Prof. Dr. H. Falcke	Max Planck institut für Radioastronomie

ISBN 90-9016817-6

The work described in this thesis is part of the research programme of the 'Nationaal Instituut voor Kernfysica en Hoge-Energie Fysica (NIKHEF)'. The author was financially supported by the 'Stichting Fundamenteel Onderzoek der Materie (FOM)'
Typeset using LaTeX2ϵ

Contents

Introduction

" Chronologically no knowledge precedes in us the experience and it's with it that everything starts"

Kant

In writing this review following books: (Ginzburg & Syrovatskii 1964, Hayakawa 1969, Longair 1981) were of great help. The existence of Cosmic Rays was revealed in 1911 by Victor F. Hess using a gold leave electroscope during balloon flights (Hess 1912), a photography taken during one of these events is shown in figure 1. The measurements revealed that the amount of ionisation in the air increased with altitude, proving the ionising radiation came from extra-terrestrial origin. Yet in the beginning it was objected that it could be the result of atmospheric disturbances like thunderstorms, and the final argument confirming the extraterrestrial source of the ionisation was given in 1925 by Robert A. Millikan, who coined the term Cosmic Ray. His argument was based on the observation made at the San Bernardino lakes (California) that the change in ionisation rate in the atmosphere and underwater are compatible with the hypothesis that the source of the ionisation comes from above. Investigations about the nature of this radiation went on ever since. At first it was believed to be electromagnetic (X-rays, γ-rays) origin, or neutral (atoms). Evidence appeared that Cosmic Rays contained a charged component, as part of them are deflected in the Earth's magnetic field, and thus their rate changes with latitude.

Figure 1: Victor F. Hess preparing for experimenting during a balloon flight, (from Pfotzer 1972).

This was observed by J. Clay who experimented with an ionisation detector while sailing over a large latitude range from Amsterdam to Java (Clay 1928). Arthur Compton (Compton 1932) also reported this effect, but it was disputed by R. A. Millikan, and a worldwide survey was organised with nine teams measuring with identical ionisation chambers at different latitudes (Compton 1933). This unambiguously proved the charged nature of Cosmic Rays.

This lead to a new question: What is the sign of the charge of this Cosmic Radiation? B. Rossi suggested to search for an east-west asymmetry at low latitudes. The Earth magnetic field bending the particles trajectory, would give rise to a shorter path length through the atmosphere for the positive charges coming-in from the east, and for the negative charged particles entering from the west. An excess from the east was observed and the Cosmic Rays had to be dominated by positively charged particles. During the same period C. D. Anderson observed Cosmic Rays secondary interactions using a cloud chamber, and discovered the positron. It resulted in 1936 in a Nobel prize shared between V. F. Hess for the discovery of Cosmic Rays and C. D. Anderson for the discovery of the positron (Anderson 1933), which almost coincided with it's prediction by P. A. M. Dirac.

From the 1930s to the 1950s, before the big particle accelerators were constructed, Cosmic Rays were the main source of discovery of new particles, such as the positron and the muon. The muon, originally called mesotron, as its mass is in between the electron and proton mass, was discovered by C. D. Anderson and S. H. Neddermeyer in 1936 using a cloud chamber (Neddermeyer & Anderson 1937). That same year H. Yukawa postulated a particle of similar mass to explain the strong interaction between protons and neutrons in a nucleus. The muon was believed to be that particle until the pion was discovered. Later, in 1947, the strange particles (K^+,K^0,K^-) were discovered in a large cloud chamber, from the observation of 'V' shaped tracks with apparently no incoming particle. G. D. Rochester, C. C. Butler and P. M. S. Blackett interpreted this as the decay of a neutral particle into two charged particles with masses of about half the proton mass (Rochester & Butler 1947). During these days the developments of the Geiger counter together with that of fast coincidence electronics allowed P. Auger, and independently W. Kolhörster to observe correlations in arrival times of particles in detectors separated by large distances, which launched the idea of Extensive Air Showers (EAS)(Auger & Maze 1939, Kolhörster, Matthes & Weber 1938).

On the astrophysical side, H. Alfvén developed the theory of magnetohydrodynamics (MHD) which describes the transport of magnetic fields by moving, electrically conducting gases, for which he received the Nobel prize in 1970. For an ideal plasma, the magnetic field moves with the fluid, and is "frozen in"(Alfvén 1943). This idea led E. Fermi to his acceleration principle for Cosmic Rays, based on multiple mirroring of energetic particles between moving magnetic clouds which act as approaching mirrors

(Fermi 1949), and it led to the general acceptance that Cosmic Rays were not only of solar origin.

Figure 2: First observation of a pion by C. Powell in 1947.

Using the developments of nuclear emulsion by the Ilford Company, C. Powell and his collaborators discovered the pions (π^+,π^-), which were the particles predicted by H. Yukawa. One of the observations is shown in figure 2, a pion comes in from the bottom left, decays to a muon and a neutrino, resulting in a kink, the muon travels to the right, to itself decay into a electron and two neutrinos. The neutral charged neutrinos do not expose the emulsion. Notice also the darkness of the tracks, the pion and muon having similar masses, have similar darkness, the electron lighter is less dark. For this discovery they received the Nobel prize in 1950. Finally, also the Ξ^- in 1952 and the Σ^0 in 1953 were discovered in Cosmic Rays. In 1953 the particle accelerators reached energies at which these particles could be produced in far larger quantities and studied with greater precision. The study of particle physics shifted to the accelerator laboratories, and the study of Cosmic Rays shifted to the study of the astrophysical sources of the radiation, and its propagation.

The Cosmic Ray spectrum

The energy spectrum of Cosmic Rays covers a very wide range with an essentially featureless power law distribution. The current knowledge of the all-particle energy distribution is shown in figure 3. Three ranges can be considered as far as the sources are concerned. The lowest energy band from $\approx$1 MeV to $\approx$10 GeV, is dominated by particles trapped in the solar wind. The variability of their rate follows the solar cycle.

The second band are the particles from Galactic sources, trapped in the galactic magnetic field. The energy of these particles essentially ranges from the solar range to the so called *knee* of the Cosmic Ray spectrum. The knee is a steepening of the spectral index of the Cosmic Ray energy spectrum at an energy estimated to be of order 3 PeV, depending on the particle species. The acceleration mechanism up to the knee is well explained by shock acceleration in supernovae remnants, beyond this energy the acceleration is more problematic to explain, as no galactic object is known to exist which could accelerate particle to these energies.

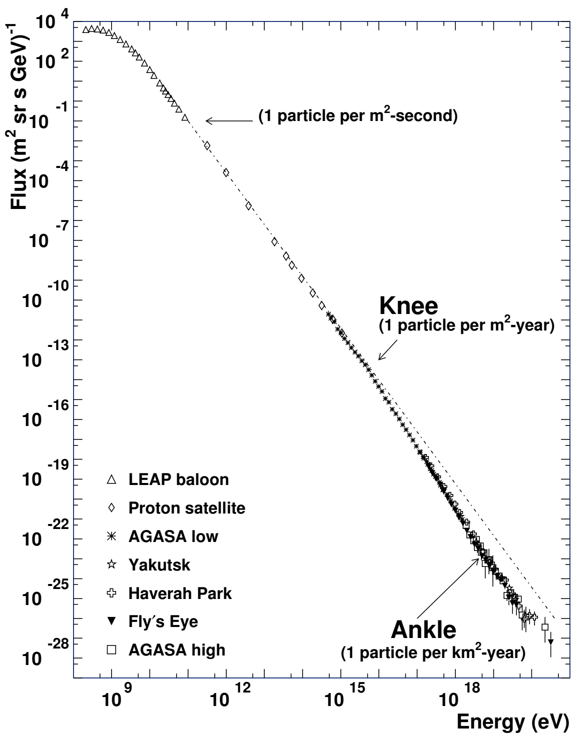

Figure 3: A survey of the all particle cosmic ray spectrum, with it's two features, the knee and the ankle. (Compilation by S. P. Swordy)

Above 1 EeV particles are considered to be of extragalactic origin, because the radius of curvature of their trajectories in the galactic magnetic field exceeds the size of the galaxy. Yet the origin of the particles beyond the knee is not yet understood as far as the acceleration mechanism bringing them to these extreme energies is concerned. Finally the Cosmic Ray energies should not exceed the energy at which they start interacting with the 2.7 K cosmic background radiation, protons would loose energy by radiation of π^0 via the Λ resonance. This effect is known as the Greisen, Zatsepin and Kuzmin or GZK, cut-off (Greisen 1966, Zatsepin & Kuzmin 1966), and would limit propagation of ultra high energy Cosmic Rays (above $3{\cdot}10^{20}$ eV) to distances of order 20 Mpc, and within this distance no suitable astrophysical source is known. Yet as early as 1963, J. Linsley reported the observation at Volcano Ranch of a Cosmic Ray induced shower of energy as high as 10^{20} eV, which is a macroscopic energy (Linsley 1963), and constitute the GZK paradox.

The Cosmic Ray composition

From the astrophysical point of view not only the energy distribution of the primary Cosmic Rays are of importance, but also the chemical composition of the Cosmic Ray flux. Comparing the relative abundances of the elements or isotopes provides information on the composition at the source location, as well as on the propagation, as some elements are not produced in standard stellar fusion processes, but only as products of spallation reactions during transport. For instance, unstable nuclei can then be produced and they are very interesting as they can be used as travelling clocks.

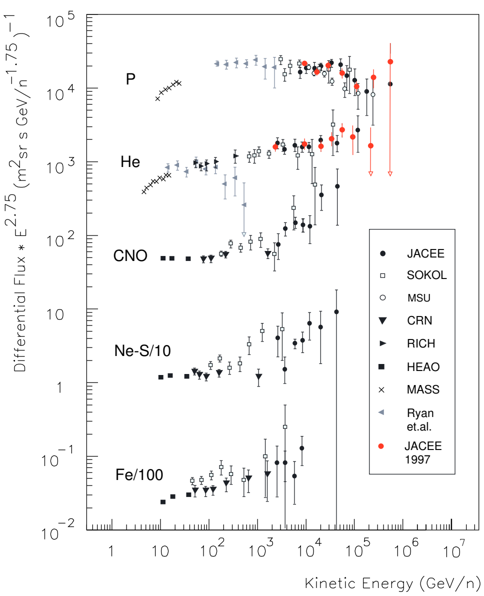

Figure 4: Current knowledge of the Cosmic Ray mass composition, in the energy range of direct measurements. Compilation from (Hinton 1998).

From the experimental point of view one can essentially distinguish two parts in the field of study of the Cosmic Ray chemical composition. The first part is the low energy domain in which the flux of a single element is high enough to be measured by direct experiments. Direct experiment are of two kinds:

- Passive detectors, like photographic emulsions, or plastics, exposed during stratospheric balloon flights. Very successful were the JACEE (JACEE Collaboration 1998) and RUNJOB (RUNJOB Collaboration 2001) programs.
- Active detectors, containing calorimeters or spectrometers and particle identification detectors, have been flown on balloons or put into near Earth orbit. Examples range from the very first PROTON experiment (Grigorov *et al.* 1971), to the very modern AMS experiment (AMS Collaboration 1994, AMS Collaboration 2000a, AMS Collaboration 2000b).

Figure 4 shows the fluxes of H, He, CNO, NeS and Fe as function of the energy per nucleon. All the spectra have a power law nature above 5 GeV/nucleon. The Fluxes have been multiplied with a power of the energy to allow better view.

In the high energy domain the fluxes are so low, of order 1 particle/m^2/year, or lower, that direct measurements are no longer possible. Only experiments with very large apertures can contribute, like Air Shower arrays, atmospheric fluorescence, or Čerenkov detectors. Since all these detection techniques do not rely on observing properties of the primary particle, but on observing properties of the particle shower they generate in the atmosphere, the estimation is not straight forward. An estimator for the mass of the primary, or more often of the logarithm of number of nucleons is used: $\ln(A)$. The later being chosen since it is proportional to observable quantities. As mentioned two schools compete: The Air Shower arrays, assess this quantity from the composition of the shower observed at ground, from the number of electrons/positrons, muons, and eventually hadrons. The fluorescence and Čerenkov detectors observe the shape of the shower as it develops through the atmosphere. A useful observable is the depth (in g/cm^2) of the shower maximum, X_{max}. This quantity depends on the total cross-section, and therefore to the $\ln(A)$. Figure 5 shows the measurements of the average $\ln(A)$ as a function of the primary energy. It is to be noticed that the X_{max} method predicts lighter compositions than the ground level observations.

Up to now electrons, γ-rays, and neutrinos have not been discussed. Their position in the study of Cosmic Rays will be shortly addressed. Electrons abundances above a few GeV are suppressed by their extremely short path length, due to their large energy loss from synchrotron radiation, the same holds for positrons. Their combined flux is of order 1% of the proton flux up to an energy of 20 GeV, then drops faster than the proton flux. γ-rays are extremely interesting, as they are not deflected by magnetic fields, most

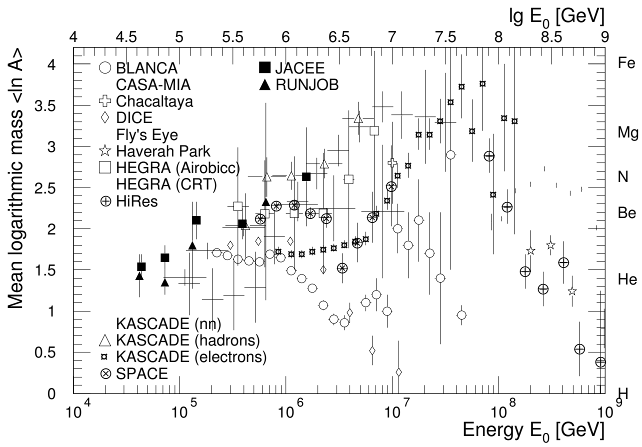

Figure 5: Estimation of the mean logarithmic mass of the primary Cosmic Ray as function of primary energy. Compilation from (Hörandel 2001).

noticeable experiments were EGRET (Hughes *et al.* 1980) and COMPTEL, flown on Comptel Gamma Ray Observatory Mission, are dedicated to observe their energy and direction. This is possible in orbit up to order 10 GeV. At higher energies the flux becomes too low. At ground the observation is very difficult, as it involves observing air showers and identifying the γ-ray induced ones with an efficiency sufficient to suppress the large excess of proton induced showers. Experiments like HEGRA (HEGRA Collaboration 1999) and Milagro (MILAGRO Collaboration 2001) have recently proved that it is possible, but the total statistics of the observations is severely limited, and simply allows one to conclude that multi-TeV photons are emitted by Cosmic Ray sources.

From the ideas of Sir A. Eddington and later the more precise formulation by H. Bethe the energy production in the Sun was understood by the reaction of four protons, creating Helium, two positrons, two neutrinos and some energy[1]. But how to test this empirically? Observing neutrinos is difficult due to their tiny cross section, only one in 10^{12} solar neutrinos would interact while traversing the earth. Fortunately they are so abundant that observations are possible. An experiment was proposed by J. N. Bahcall and R. Davies to test the proton fusion hypothesis, using 380 m^3 of chlorine based

[1]For completeness it should be mentioned that next to the direct process, a second process dominates in stars heavier than the Sun: the CNO cycle, in a revolution of the cycle 4 protons get fused into a Helium, using ^{12}C as a catalyst.

cleaning fluid (perchlorethylene). An interacting neutrino may transform a chlorine nucleus into a argon isotope, which can be filtered out. It confirmed in 1968 that fusion was taking place in the Sun, but it also exposed the solar neutrino problem, less argon was observed than expected. Many experiments have confirmed this discrepancy and many models were created to explain it, lets just remember the proposition by B. Pontecorvo and V. Gribov that neutrinos may be oscillating between an easily observable state and a second state, more difficult to observe.

A second source of neutrinos are the atmospheric neutrinos, they are produced in the decay of a charged pion into a muon and a neutrino, and in the subsequent decay of this muon into an electron or a positron and two neutrinos. Measurements on these neutrinos by the Super-Kamiokande collaboration, allowed them in 1998 to claim the observation of neutrino oscillations (Fukuda *et al.* 1998). In the light of the search for neutrino oscillations, the L3+C experiment was proposed. Its primary goal was the precise measurement of the atmospheric muon spectrum, which knowledge constrains the predictions on the atmospheric neutrino spectrum. This confirmation earned R. Davies & M. Koshiba the Nobel prize in 2003.

A last set of neutrinos of interest are the very high energy neutrinos, either from astrophysical sources, or relics from the early universe. The detection of these neutrinos, far less abundant than the solar or the atmospheric ones, requires the instrumentation of very large detection volumes. The sizes needed are too large to fit in human constructions, and lake Baikal (Bagduev *et al.* 1999, Balkanov *et al.* 2002), the Mediterranean sea (ANTARES Collaboration 2002, NESTOR Collaboration 2001) and Antarctic ice (AMANDA Collaboration 2000, Halzen *et al.* 1999) are and will be used. The experimental technology invariantly being the collection of the Čerenkov light emitted by the charged products of an interaction between the neutrino and the water target.

Coming back to Cosmic Ray of hadronic nature, the L3+C experiment with an Air Shower Array, and a muon detector at a medium depth, not as deep as the MACRO or LVD detectors, compared to the EAS-TOP array (Macro and EAS-TOP Collaborations 1994, LVD and EAS-TOP Collaborations 1998) or the Soudan-2 detector (Longley *et al.* 1995, Kasahara *et al.* 1997) compared to their surface proportional counters, were the uncertainty in the overburden is to be taken into account, and not as shallow as the muon tunnel installed in the KASCADE array (KASCADE Collaboration 2001a) or the MIA muon detector with respect to the CASA array (Borione *et al.* 1994), which is mainly sensitive to low energy muons produced in the late stages of the cascade, constitute an apparatus in a new domain. Thanks to the small size of the array, it is sensitive in a range overlapping with the JACEE and RUNJOB measurements, and extending to the knee. The muon energy threshold of about 18 GeV allows it to probe muons originating from the first stages of the cascade. Therefore it is an ideal instrument to study the high energy Cosmic Ray interactions.

In this work, the first chapter will briefly sketch the astrophysics of Cosmic Rays in the Galaxy. The second chapter discusses the development of Air Showers with a main emphasis on the models for strong interactions used for Cosmic Rays interactions as they constitute the main source of uncertainty in the understanding of the Air Shower development through the atmosphere. In chapter 3 the muon detector and the Air Shower detector are described followed in chapter 4 by the description of the reconstruction methods used to obtain the interesting physics quantities from the detector readouts. In chapter 5 the selections which are to be applied to improve the quality of these quantities are presented, and in the last chapter a comparison between the measurements and the expectations from different models will be performed, revealing major problems in the prediction on particle production, which prevents any interpretation in terms of Cosmic Ray composition. The measurements will be presented in an apparatus independent fashion in order to provide input for improvement on the Cosmic Ray interaction models.

Chapter 1

Particle acceleration and propagation

In this chapter only the basic ingredients of Cosmic Ray acceleration and propagation are sketched, as a thorough description would be a book of its own. The reader is invited to read the founding monograph (Ginzburg & Syrovatskii 1964) for all the details. A contemporary formulation can be found in (Kirk 1994, Achterberg 1997). Particle acceleration and propagation through the galaxy can be summarised by a formal equation, each term of which describes one of the essential processes or contributions.

$$\begin{aligned} &\frac{\partial N_i}{\partial t} - \mathrm{div}(D_i \nabla N_i) + \frac{\partial}{\partial E}(b_i N_i) - \frac{1}{2}\frac{\partial^2}{\partial E^2}(d_i N_i) = \\ &Q(E, \mathbf{r}, t) - p_i N_i + \sum_k \int P_{k \to i}(E, E') N_k(E', \mathbf{r}, t) dE' \end{aligned} \tag{1.1}$$

N_i Density of Cosmic Rays of species i of energy E at position $\mathbf{r}$ and at time t.

D_i Diffusion coefficient for species i.

b_i Coefficient for continuous energy variations.

d_i Coefficient for stochastic energy variations.

Q Distribution of the Cosmic Ray sources.

p_i Disappearance rate of the Cosmic Ray species i.

$P_{k\to i}$ Rate of production of species i by species k.

The first term on the left hand side, $\frac{\partial N_i}{\partial t}$, describes the time variation of the cosmic ray density. The density is usually supposed to be constant, as the time scale at which Cosmic Ray leave is of order 10^8 years, while their production is governed by SNRs which evolve at the time scale of 10^4 years. Yet a decrease of the Cosmic Ray intensity over time has been reported (Stozhkov, Okhlopkov & Pokrevsky 2001). This has been interpreted as related to the Cosmic Ray flux induced by a nearby Super Nova, whose particles are diffusing away from the neighbourhood of the Earth.

The second term $\mathrm{div}(D_i \nabla N_i)$, is the spatial diffusion term and includes losses from the Galaxy. It includes different diffusion coefficients D_i for each species of Cosmic Ray i. This coefficient is related to the presence of inhomogeneities in the galactic magnetic field. Also, the diffusion coefficient depends on the energy, but this dependence is only of importance when the radius of curvature of the particle trajectory reaches galactic scales, i.e. for $E \gtrsim 1\, PeV$. Above these energies the coefficient depends on the charge to mass ratio, which creates mainly two main cases the protons and the heavier elements. The electrons do not travel very far at such energies as they loose energy by pair creation on the 2.7 K background radiation.

The third term, $\frac{\partial}{\partial E}(b_i N_i)$, describe energy changes (losses) in small increments. One can think here of ionisation and bremsstrahlung energy losses, and in regions of high magnetic fields of synchrotron radiation plays a significant role. The term also includes systematic acceleration where $b_i(E) = \frac{dE}{dt}$ is the energy increase per unit time.

The fourth term, $\frac{1}{2}\frac{\partial^2}{\partial E^2}(d_i N_i)$ also describes diffusive energy transfer, but from stochastic processes. In here the coefficient $d_i(E)$ is given by $d_i(E) = \frac{d}{dt}\overline{(\Delta E)^2}$. $\overline{(\Delta E)^2}$ is the variance of the energy increments.

On the right hand side, the first term describes an injection term of Cosmic Rays, typically Supernova remnants, but also near compact objects such as radio pulsars and black holes. At lower energies near flair stars including the Sun. The second term is the disappearance rate of the Cosmic Rays, this can be due to decay for unstable particles, or absorption in the interstellar medium. If the decay produces particles of another species of interest, then it should be accounted for in the last term, which is the rate of species changing reactions. For instance spallation of species k upon the interstellar medium forming species i would contribute to such term.

1.1 Induction acceleration

To accelerate charged particles to high energy, the only solution is to have electric fields acting over large distances. The universe is globally uncharged so large scale static electric fields do not exist. However one can get electric fields by induction from magnetic fields which are known to exist on large scales in the universe.

Lets consider a region in which the magnetic field is uniform at the scale of the particle radius of curvature. If the magnetic field strength increases in time, the particle of charge q experiences an induced electric field $\mathbf{E}$ and the energy gain ΔE in one revolution is:

$$\Delta E = q \int \mathbf{E} \cdot d\mathbf{l} \approx \oint \mathbf{E} \cdot d\mathbf{l} = \frac{|q|}{c} \frac{\partial \Phi}{\partial t} \tag{1.2}$$

Where Φ is the magnetic flux enclosed in the particles trajectory. It is important to notice that since the acceleration is continuous and doesn't involve collisions with particles this mechanism is able to accelerate heavy ions without breaking them.

1.2 The colliding magnetic wall acceleration

This is a variation on the previous theme. This time a particle with velocity $\mathbf{v}$ encounters a magnetic wall travelling with velocity $\mathbf{u}$. Figure 1.1 gives an impression of such a event. The particle will experience an induced electric field $\mathbf{E} = \frac{-1}{c}\mathbf{u} \wedge \mathbf{H}$.

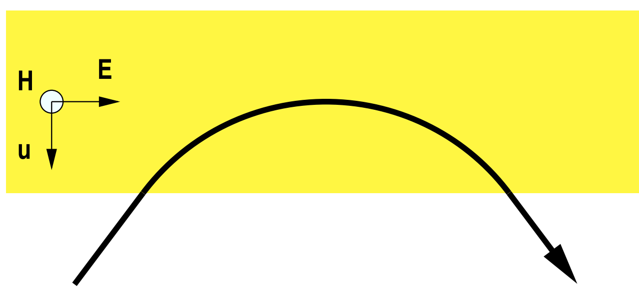

Figure 1.1: Collisions of a particle with a moving magnetic wall.

The energy gained in the process is:

$$\begin{aligned} \Delta E &= q \int (\mathbf{E} \cdot d\mathbf{s}) \\ &= \frac{2E}{c^2}(\mathbf{u} \cdot \mathbf{v}) \end{aligned} \tag{1.3}$$

which is proportional to the energy of the particle.

1.3 Fermi acceleration

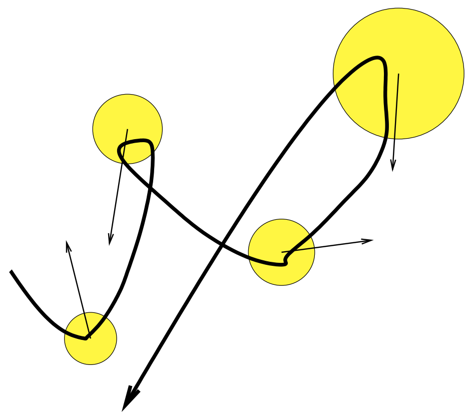

Figure 1.2: Illustration of fermi acceleration: A particle collides with regions of high magnetic fields traped in moving plasma clouds.

The acceleration principle is based on the probability of a head on collision being higher than an overtaking collision. This results in a net energy increase per unit time proportional to the energy of the particle. Finding a stationary solution to equation (1.1), neglecting diffusion and in absence of sources, assuming the particle stays in the region for a characteristic time τ, the equation becomes:

$$-\frac{\partial}{\partial E}(\alpha E N(E)) - \frac{N(E)}{\tau} = 0 \tag{1.4}$$

and has as solution:

$$N(E) = N_0 E^{-(1+\alpha^{-1}\tau^{-1})} \tag{1.5}$$

where $\alpha = \int \frac{2(\mathbf{u}\cdot\mathbf{v})}{c^2} P(\mathbf{v}) d^3 v$. is expressed in terms of the probability per unit time of collision with an inhomogeneity of velocity $\mathbf{v}$.

This derivation did not take into account the acceleration due to the fluctuations. It is not difficult to establish the parameter d_i:

$$d_i = \int \frac{4(\mathbf{u}\cdot\mathbf{v})^2 E^2}{c^4} P(\mathbf{v}) d^3 v = \delta E^2 \tag{1.6}$$

And taking it into equation (1.1), modifies the solution into:

$$N(E) = N_0 E^{-\frac{1}{2}\left[3-\frac{\alpha}{\delta} \pm \sqrt{\left(1-\frac{\alpha}{\delta}\right)^2+\frac{4}{\delta\tau}}\right]} \tag{1.7}$$

For simplicity let us discuss solution (1.5). When the velocities of the inhomogeneities are small, the acceleration mechanism is very inefficient due to the term $(v/c)^2$ in α[1], considering that the speed of the plasma blobs ejected by a supernova are of the order 10^4 km/s. This requires very long confinement times to explain the observed spectrum. Therefore Bell (Bell 1978), and Blandford & Ostriker suggested a more efficient solution:

1.4 Strong shock acceleration

A shock front appears in the explosion of a supernova, as the speed of expelled particles exceeds by far the speed of sound in the static interstellar medium. The relativistic Cosmic Rays in front of the shock have isotropic distribution due to the scatterings on the inhomogeneities. After the passage of the shock, scatterings will randomise the directions again, but now with respect to the flowing gas, thus acquiring kinetic energy from it. As the Cosmic Rays are highly relativistic some of them will overtake the shock front going back to the static interstellar medium, and with time randomise their direction again. The expanding shock will catch up again and the process gets repeated. The details of the model can for instance be found in (Longair 1981). The model predicts that:

$$N(E) = N_0 E^{-2} \tag{1.8}$$

This process has to stop when the particles are so energetic that they can't be kept in the vicinity of the shock. To quantify this lets compare the giromagnetic radius to the size of the supernova remnant of order R =1 pc, with a magnetic field strength of order H =10 μG, thus giving the maximum energy of order 10^{15} eV. Coincidentally this is the energy of the knee in the Cosmic Rays energy spectrum.

$$E_{max}(\text{eV}) \approx 300\text{R(cm)H(G)} \tag{1.9}$$

Figure 1.3 shows an optical observation by the Hubble Space Telescope of the Crab nebulae, which is the remnant of the July 4th 1054 supernova, and an established source of Cosmic Ray. The turbulent gas flow discussed above can clearly be seen.

[1]One factor v/c is explicit in the expression of α, the second is hidden in the integration of the scalar product weighted by the probability

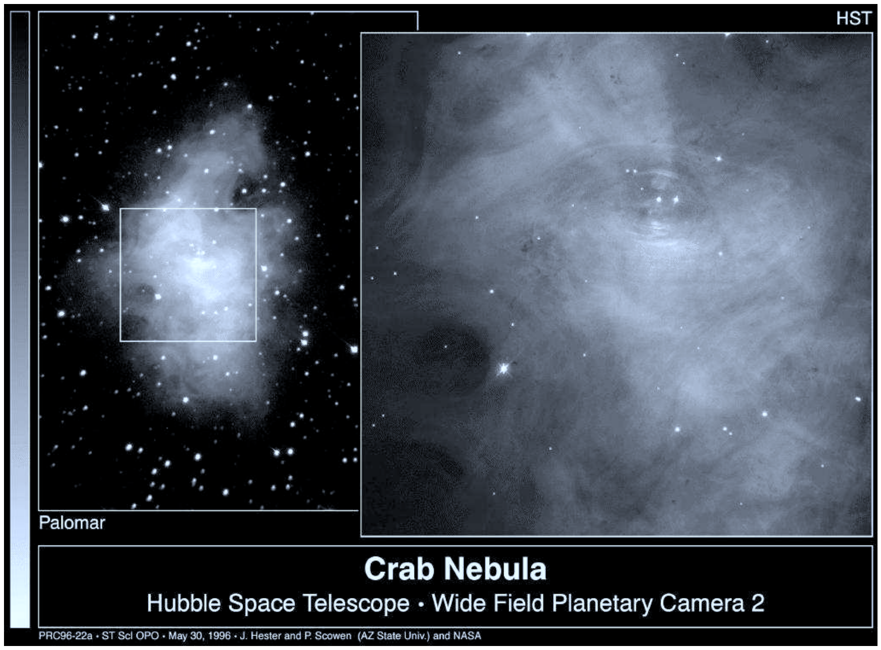

Figure 1.3: Photography of the Crab supernova remnant, taken with the Hubble Space Telescope. (Source NASA)

This short discussion on Cosmic Ray acceleration will be closed after presenting the candidates for producing particles beyond the above mentioned maximum energy. The source region should either have far stronger magnetic fields or extend to far larger regions of space. This makes Active Galactic Nuclei natural candidates. Acceleration in the radio lobes of active galaxies is considered in (Micono, Zurlo, Massaglia, Ferrari & Melrose 1999) and alternatively the shock front created by the gravitational collapse of the gases outside the local cluster onto it. In (Sangjin, Angela & Guenter 1995) the suggestion is made to use these highest energy Cosmic Rays to probe the existence of extragalactic magnetic fields.

Chapter 2

Extensive air showers

> "Les termes symboliques qui relient une loi de physique ne sont plus de ces abstractions qui jaillissent spontanément de la réalité concrète, ce sont des abstractions produite par un travail lent, compliqué, conscient, par le travail séculaire qui a élaboré les théories physiques"
>
> P. Duhen

The understanding of the development of an Air Shower in the atmosphere requires knowledge about interactions of nuclei at very high energy and knowledge of the transport of their products through the atmosphere. The latter part is very well understood, as it has been precisely studied in the laboratory, and is mainly governed by Quantum Electro Dynamics (QED) which gives high precision predictions. The first part is far less understood. This part is governed by Quantum Chromo Dynamics (QCD) which, being predictive at high energy scales thanks to perturbative calculations, fails at low energy scales where an expression of cross sections in power series of the coupling constant converges too slowly.

The model makers are faced with the difficult task to heuristically describe the experimental data, and to extrapolate this to energy scales far beyond existing measurements. For these extrapolations to work, they try to include as much of the understood physics as possible. In Figure 2.1 the three components of such models can be seen. On the left, one question to be solved is how many quarks and gluons, (which are collectively named is partons), compose the incoming hadrons. This composition is described by the structure functions, and their knowledge has greatly improved in recent years for the protons from the deep inelastic scattering experiments at HERA. The second part (indicated in the dashed circle) are the hard scatterings, which are described using perturbative QCD. The last part is the least understood, hadronisation,

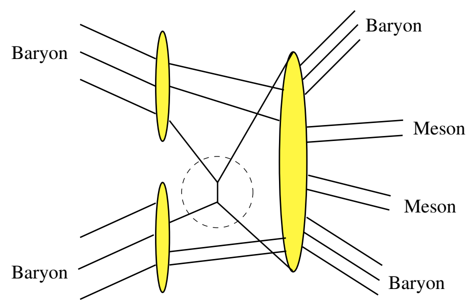

Figure 2.1: Example of a baryon baryon collision. The area in the dashed circle shows the perturbative QCD part, the large grey area the hadronisation part.

where nature takes care that only colour-neutral charged particles appear in the final state.

2.1 Introduction to QCD.

As the quote at the start of this chapter suggests, modern theoretical physics is the work of many, this is all the more true for QCD. From the original discovery of non-abelian gauge theories by Yang and Mills, and later the proof of their renormalisability by 't Hooft and Veltman. Passing by the introduction of partons by Björken to describe the 1968 SLAC data, and the invention of quarks by Gell-Mann, to explain the symmetries between hadrons. Stopping to underline the work of Altarelli and Parisi, and learning how to deal with ghosts from Fadeev and Popov, we get to the modern formulation of QCD presented in the coming subsections, having forgotten to acknowledge the contributions of many others.

2.1.1 The Lagrangian

The strong force is described by a theory based on local gauge invariance under SU(3) transformations of the quark Lagrangian[1]:

$$\mathcal{L}_{QCD} = \bar{\psi}^a_{\mathrm{q}}(i\gamma^\mu D_\mu - m_{\mathrm{q}})_{ab}\psi^b_{\mathrm{q}} + \frac{1}{4}F^A_{\mu\nu}F^{A\mu\nu} \tag{2.1}$$

[1] Any set of repeated indexes implies an implicit sum

Where ψ_q^a are the eighteen spinors associated to the three colour charges of the six quarks. The covariant derivative D_μ in terms of the eight gluon fields G_μ^A is given by:

$$D_{ab,\mu} = \partial_\mu \delta_{ab} + i\sqrt{4\pi\alpha_S}\, G_\mu^A T_{ab}^A$$

and the field strength tensor $F^{A\mu\nu}$ is:

$$F_{\mu\nu}^A = \partial_\mu G_\nu^A - \partial_\nu G_\mu^A - \sqrt{4\pi\alpha_S}\, f^{ABC} G_\mu^B G_\nu^C$$

with T_{bc}^A and f^{ABC} being the SU(3) generators and structure constants, respectively.

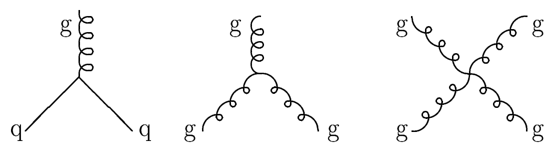

Figure 2.2: Vertexes predicted by the QCD Lagrangian.

This Lagrangian generates three elementary vertexes, shown in Figure 2.2. The predictions of the cross sections for the qq→ qq, qg → qg, qq → gg and gg → gg scattering is tedious but straightforward, at the first orders in the strong coupling constant α_S.

2.1.2 Evolution of the coupling constant

The critical point of the QCD Lagrangian is that, when working out the renormalised theory, one finds the evolution of the coupling constant to follow equation (2.2), in which N_f is the

$$\alpha_S(Q^2) = \frac{4\pi}{(11 - \frac{2}{3}N_f)\ln\frac{Q^2}{\Lambda^2}} + O\left(\frac{\ln\ln\frac{Q^2}{\Lambda^2}}{(\ln\frac{Q^2}{\Lambda^2})^2}\right) \tag{2.2}$$

number of quark flavours. As long as the number of flavours is less than 17, the coupling strength decreases with the energy scale, which is known as asymptotic freedom. This also means that at energy transfer scales close to the scale factor Λ, the coupling constant is close to unity, and the perturbative approach fails. Experimentally Λ is determined to be of order 200 MeV. The precise definition of Λ depends on the renormalisation scheme used. Figure 2.3 shows measurements of α_S at different energy scales, compared with the predicted evolution. Other approaches have to be used in order to predict hadron-hadron processes.

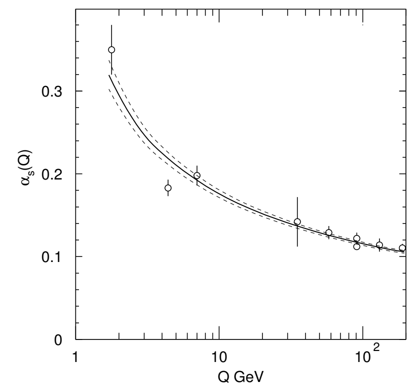

Figure 2.3: Summary of the values of $\alpha_s(Q)$ at the value of the scale Q they are measured (Hagiwara *et al.* 2002).

2.1.3 Structure functions

The proton or the neutron, contrary to the electron, are composite objects. At a first approximation they are composed by three quarks, called valence quarks. Yet the situation is not as simple. Depending at the scale the constitution of the nucleons is probed the number of constituents changes, becoming larger and larger at smaller distances, or equivalently at larger energies. The growing number of additional constituents carry smaller and smaller fractions of the total momentum. The evolution of the number of constituent, as function of the observation scale Q^2, and the fraction of the momentum carried by the constituents x, is studied in deep inelastic scattering experiments, first performed at SLAC in the sixties, reached high precision at the DESY collider in resent years. The interested reader is referred to (Tuning 2001) for the details of the measurement performed at the ZEUS detector, where the proton is probed with high energy photons or weak gauge bosons, produced from positrons. The recent measurements at HERA extended by more than one order of magnitude in Q^2, and by more than one order of magnitude down in x the knowledge of the structure functions. The interaction models used in cosmic rays have been updated to this new measurements. The either have there own parametrisation based on the data, or use parametrisations from expert groups like CETQ (Coordinated Theoretical-Experimental project on QCD). Table 2.1

shows how the different models implemented the parton density functions.

Model	Parton densities		structure functions		Saturation
	From "Expert group"	Explicit calculation	pre-HERA	post-HERA	
DPMJET	X			X	Yes
QGSjet		X	X		No
NeXus		X		X	3.0
SIBYL	X		1.7	2.1	2.x

Table 2.1: Choices made for the different model in their implementtaion of the parton density functions.

At very small x the parton densities increase rapidly. It is discussed in (Gribov, Levin & Ryskin 1983) that at the large parton numbers, parton-parton interactions will effectively screen the total number of partons. This effect is called saturation and table 2.1 indicates which models includes a description of this effect.

2.2 Models for strong interactions

In the following the Mandelstam variables defined for two-body interactions with incoming momenta p_1 and p_2, and outgoing momenta p_3 and p_4 will be used. They are $s = (p_1 + p_2)^2$, $t = (p_1 - p_3)^2$ and $u = (p_1 - p_4)^2$. These Lorentz invariant quantities add up to $s + t + u = m_1^2 + m_2^2 + m_3^2 + m_4^2$.

2.2.1 Parton Model

The parton model considers the inclusive cross sections of partons of species i and j, which are constituents of the projectile hadron h_1 and the target hadron h_2, respectively. These cross sections are summed over the species of partons and weighted by the momentum distributions f_{h_1} and f_{h_2} of the partons inside the hadrons. Calculating the inclusive cross section, at a squared centre of mass energy, for the production of parton induced jets with squared transverse momentum $p_\perp^2$ above some cutoff scale Q_0^2 one obtains:

$$\sigma_{incl}^{h_1,h_2} = \sum_{ij} \int dp_\perp^2 \int dx_1 \int dx_2 f_{h_1}^i(x_1, p_\perp^2) f_{h_2}^j(x_2, p_\perp^2) \frac{d\sigma_{ij}}{dp_\perp^2}(x_1, x_2, s)\theta(p_\perp^2 - Q_0^2) \tag{2.3}$$

The variable x is the fraction of the hadron momentum carried by the parton. This approach is well suited to describe the central region, i.e. the region of large transverse momenta. Therefore it is applied in the Monte Carlo models used in collider experiments, PYTHIA and HERWIG. In fact multiple scatterings take place within a single collision. This is taken into account by defining the m-scatterings cross section:

$$\sigma_m^{h_1,h_2} = \int d^2bP\left(m|A(b)\sigma_{incl}^{h_1,h_2}(s)\right) \tag{2.4}$$

Where $A(b)$ is the hadron-hadron overlap function at impact parameter b, and P is the Poisson probability. To get the inelastic cross section one sums over all m:

$$\sigma_{inel}^{h_1,h_2} = \sum_{m>0} \sigma_m^{h_1,h_2} = \int d^2b\left(1 - \exp\left(-A(b)\sigma_{incl}^{h_1,h_2}(s)\right)\right) \tag{2.5}$$

This factorisation called eikonalisation, has several flaws. For instance it does not take into account non-factorisable contributions. Also, the sharing of the energy is not taken into account. Furthermore the models have ad-hoc implementations of energy conservation. Finally, it is not obvious how it has to be extended to nucleus-nucleus collisions, as far as re-scattering is concerned.

2.2.2 Gribov-Regge theory

GRT is a phenomenological approach to hadron-hadron scatterings, described by the exchange of objects called reggeons or pomerons. Their properties are derived from basic assumptions about the properties of the scattering matrix, such as unitarity and analyticity. The parameters of the model are adjusted to the experimental data on the forward scattering, and the total cross-section. GRT has regained a large interest in the models suited for Cosmic Ray interactions, where a correct description of the energy flow, and of the leading particles is of high importance.

Optical theorem

The optical theorem uses the unitarity of the scattering matrix. It states that the part of the flux which is not elastically scattered goes to other channels. It relates the forward elastic scattering at small angles in the centre of mass frame with the total cross section. Its use allows to extract the total cross section from a measurement of the elastic scattering.

For instance total cross section, for pp collisions:

$$\sigma_{tot} = \frac{1}{\Phi}\int dP_X |M_{pp\to X}|^2 \tag{2.6}$$

$$= \frac{1}{\Phi}\int dP_X M_{pp\to X} M^{\dagger}_{pp\to X} \tag{2.7}$$

Where the $M_{pp\to X}$ are the matrix elements for proton proton to any of the possible final state X. Φ is the incoming flux. Each phase space integration results into a particle propagator:

$$\frac{d^3k}{2E} = \delta\left(k^2 - m^2\right) d^4k \tag{2.8}$$

$$\propto \Im m\left(\frac{1}{k^2 - m^2 + i\epsilon}\right) d^4k$$

We get the optical theorem, relating the amplitude for elastic scattering $A_{pp\to pp}$, to the total cross section. The elastic scattering has to be evaluated at zero square momentum transfer ($t = 0$), and

$$\frac{1}{s}\Im m A_{pp\to pp}(s, t = 0) = \frac{1}{\Phi}\int dP_X |M_{pp\to X}|^2 = \sigma_{tot} \tag{2.9}$$

Graphically interpreted, the theorems proof can be seen from Figure 2.4.

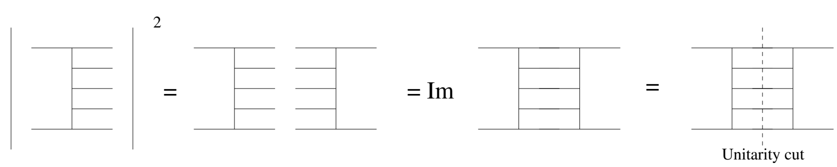

Figure 2.4: Interpretation of the optical theorem, from left to right are equations (2.6) (2.7), equation (2.8) allows closeing the lines if one takes the imaginary part.

Reggeons and Pomerons

To introduce the concept of a reggeon, the simplest is to consider a meson-meson scattering like on left of figure 2.6. The two valence quarks are of opposite colour charge. In between them the region is filled with the colour-field. It has to be noticed that the topology of this field is planar. Also, when the unitarity-cut is applied (right part of the figure) quantum numbers are exchanged. This exchange of quantum numbers makes the reggeon difficult to use for more complicated diagrams. One has to notice that the result of the unitarity-cut is the fragmentation of one string.

It would be interesting to have an object exchanged with the quantum numbers of the vacuum. This is achieved with the pomeron. In figure 2.7, on the left side, the exchange between the two mesons involves a colour-field configuration which has a cylindrical topology. Applying the unitarity-cut (right hand side of the figure), one obtains the fragmentation of two strings. The pomeron has appealing properties related to summing or factorising, in the evaluation of complicated diagrams.

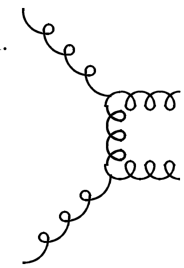

Figure 2.5: Parton interpretation of the pomeron.

It is important not to give too fundamental meaning to these concepts as the propagator associated to them is heuristic, and chosen so as to describe experimental data. But an interpretation in terms of partons exists for the cut pomeron, as a two gluon splitting, like shown in figure 2.5. The Amplitude associated with the elastic exchange of a single pomeron is parametrised as:

$$T(s,t) \propto i \exp((A + Bt) \ln s) \tag{2.10}$$

The fragmentation probability of a pomeron is uniquely given by Gribov-Regge theory, and common to all models based on this theory. But the parameters A and B are tuned, so as to get the expected total proton-proton cross-section, as well as the expected ratio of elastic to inelastic scatterings in the forward region. Applying the optical theorem one reads:

$$\sigma_{tot}(s) = \frac{1}{s}\Im m T(s, t = 0) \tag{2.11}$$

$$= \int \frac{1}{s}\Im m \tilde{T}(s, b) \mathrm{d}^2 b \tag{2.12}$$

Where b is the impact parameter, and using $t = -p_\perp^2$, $\tilde{T}$ is the Fourrier transform of the amplitude.

2.2.3 Semi hard QCD

Models used to describe Cosmic Rays interactions must be able to describe correctly the particle multiplicities but also the energy flow of nucleon-nucleus and nucleus-nucleus interactions. All models considered implement the parton model above a momentum transfer scale $Q_0 \gg \Lambda_{QCD}$. For the low momentum transfer region models

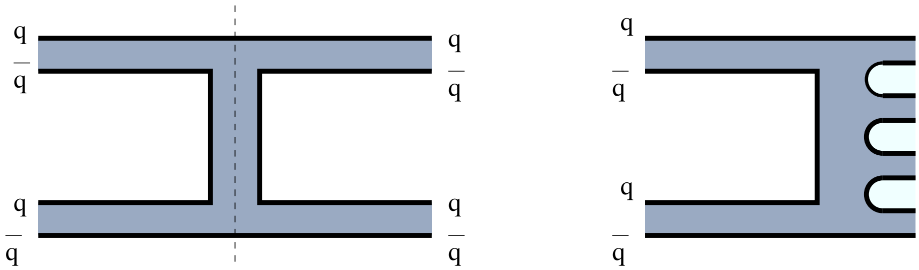

Figure 2.6: Illustration of a reggeon.

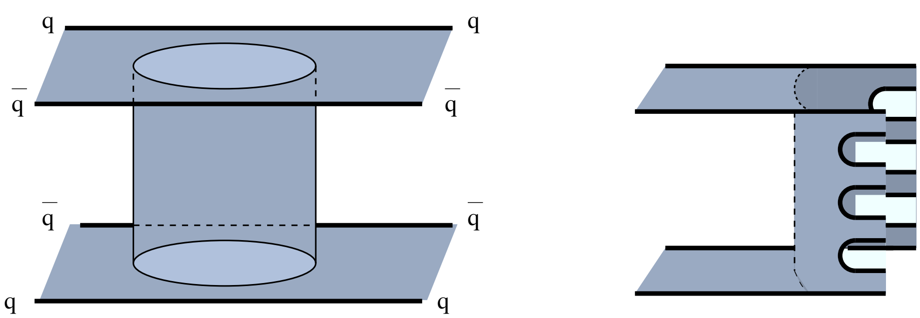

Figure 2.7: Illustration of a pomeron.

either implement the pomeron model in QGSjet (Kalmykov, Ostapchenko & Pavlov 1997) and VENUS (Ostapchenko, Thouw & Werner 1997), or the Dual Parton Model in DPMjet (Ranft 1995) and SIBYLL (Fletcher, Gaisser, Lipari & Stanev 1994). The dual parton model describes the nucleons as composed of a quark in a colour triplet and a diquark in a colour antitriplet state. Soft gluons transmit the interaction between two nucleons, ending up as in the pomeron case in the fragmentation of two stings. This is not conceptually very different from the pomeron model.

All models proceed in the following way. They introduce an eikonal function:

$$\chi(b, s) = \chi_{soft}(b, s) + \chi_{hard}(b, s) \tag{2.13}$$

Composed of the soft pomerons or strings and the hard parton based contribution. By eikonalisation, to introduce multiple scatterings, one gets the elastic scattering amplitude as:

$$T(s,t) = \frac{i}{2\pi} \int d^2 b e^{i\mathbf{p}_\perp \cdot \mathbf{b}} \left(1 - e^{-\chi(b,s)}\right) \tag{2.14}$$

And the inelastic cross section is given by:

$$\sigma_{\text{inel}} = \int d^2 b \left(1 - e^{-2\chi(b,s)}\right) \tag{2.15}$$

The distinctions between the models are then threefold. First their choice in the parameters they used in $\chi_{soft}(b, s)$. Second the choice of the momentum transfer scale Q_0. Last the parametrisation used for the structure functions in the hard part.

A more subtle mixture of the pomeron and parton description of strong interaction is investigated in the model NeXus (Drescher, Haldik, Ostapchenko, Pierog & Werner 2001). Unfortunately this model requires an order of magnitude more computer time to generate events, and could not be used in the context of this work.

2.2.4 From nucleon to nucleus: Gribov-Glauber

Up to now only the nucleon-nucleon case was discussed. In Cosmic Ray interactions the most likely target is not an isolated nucleon, but a nitrogen nucleus. The most naive approach to handle this problem, is that of the superposition model, considering a nucleus of atomic mass A as a packet of A completely independent nucleons, each interacting without influencing any of the spectators. The development of the shower would then follow an exponential shape based on the interaction length of a single nucleon. This is unsatisfactory and the Gribov-Glauber formalism gives a more elegant formulation. The idea is very similar as to how multiple scatterings have been introduced in the parton model, but instead of considering partons inside the nucleon, now nucleons are considered in the nucleus.

All models use this framework to decide the number of nucleons from the projectile which interact inelastically. The energy deposited by the scattering products in the remainder of the projectile is estimated, and then remainder is fragmented according to the energy it received. The interested reader is referred to the detailed description of the models for the details of each implementation.

2.2.5 Cross-sections

Figure 2.8 shows the predictions on the inelastic cross-section for p-Air collisions. They are compared to the estimations of the cross-sections extracted from measure-

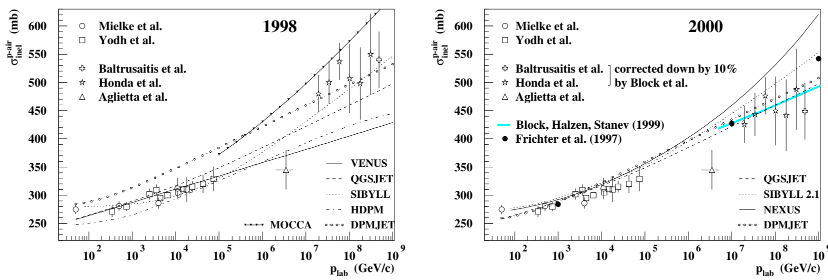

(a) Situation in 1998

(b) Situation in 2000

Figure 2.8: Inelastic p-Air cross-sections. Predictions from models compared with measurements of the cross-section extracted from the attenuation length in the atmosphere, from (Swordy *et al.* 2002).

ments of the attenuation length (Λ) of air showers in the atmosphere, using the relation:

$$\Lambda = k \frac{14.6 m_p}{\sigma_{ine}^{p-air}} \tag{2.16}$$

Where k is related to the average in-elasticity, which in Gribov-Regge Theory is predicted as the string fragmentation probabilities, fixed by the underlying physics. Yet each model has its own underlying physics as described previously, and not all data sets used the same values, hence the correction by Block in figure 2.8b. Explaining the convergence of the predictions between 1998 and 2000, the main source is the improvement on the knowledge of the parton structure functions from the HERA experiments.

2.3 Shower development

With a model for the strong interactions, the description of the development of an Air Shower through the atmosphere is not complete. One needs a transport code which should describe the density and composition of the atmosphere, and propagate the primary particle and secondaries taking into account all known physics about the passage of particles through matter. There is a chapter of the Particle Data Book (Hagiwara *et al.* 2002) dedicated to this issue which is of great help to any experimental physicist.

Also the decay of unstable particles, and the low energy nuclear interactions should be considered. There are many implementations of such code, like COSMOS, TARGET, CORSIKA (Heck & Knapp 2001, Heck, Knapp, Capdevielle, Schatz & Thouw 1998). The latter is very popular, first developed for the KASCADE experiment (KASCADE Collaboration 2001a) it was adopted by many experiments, because of its flexibility. In this work it is the version 6.04 of the program which is used.

The electromagnetic interactions are fully described by the EGS4 code (Nelson, Hirayama & Rogers 1985). Its high precision makes it very popular to calculated dosimetry in medical applications. CORSIKA also allows an analytic approximation to the electro-magnetic shower development called NKG, but this was not used in this work.

For the nuclear part of the cascade (below 80 GeV), the GEISHA code was used, which is also used in the GEANT detector simulation package (Brun *et al.* 1994). There is an alternative choice called URQMD (Bleicher *et al.* 1999, Bass *et al.* 1998), unfortunately the CPU usage of this code restricted the author from using it.

The description of the atmosphere used in this work was the standard U.S. atmosphere parametrised by J. Linsley. A good impression of the complexity of an Air Shower can be seen in figure 2.9, obtained with the CORSIKA code.

2.4 Shower simulations

In this section the shower simulation process in described. The philosophy is to have exactly the same reconstruction and analysis on the data and the simulation. CORSIKA used to simulate the propagation of the particles up to the altitude of Air Shower array. From there dedicated programs take over. One part uses the charged particles crossing the Air Shower array modules to simulate a detector response, in terms of trigger timing and pulse charge. These quantities are then reconstructed in exactly the same algorithm as used for data. The muons likely to reach the muon detector are tracked through a GEANT description of the detector and surroundings. The response of the detector is simulated ad the output produce is similar to the data produce by the real readout system. The same algorithm is then used to reconstruct the real data and the simulated data.

For each of the interaction models, DPMJET, QGSJET, SIBYLL and VENUS, shower initiated by protons and by iron were produced. In all cases a spectral index of -2.7 was used. The showers direction range from vertical to 60° inclination. The number of events generated in the proton case amounts to 15 million showers above 5 TeV for each model, and to 2.5 million showers above 50 TeV for the iron case. All charged particle are tracked till their energy reaches 2 MeV, which corresponds to the energy threshold needed to deposit a signal in the modules of the Air Shower Array.

The shower cores were distributed randomly on a $70{\times}70\,\mathrm{m}^2$ surface. On the sampling surface, a virtual square tilling was laid, with same pitch as the square surface on which the shower cores are distributed. In each of the tiles the simulation of the detectors is performed, if the requirements for a trigger are fulfilled, this defines an event. In this way the shower are sampled at all distances from the core, without reusing the same particle in different events.

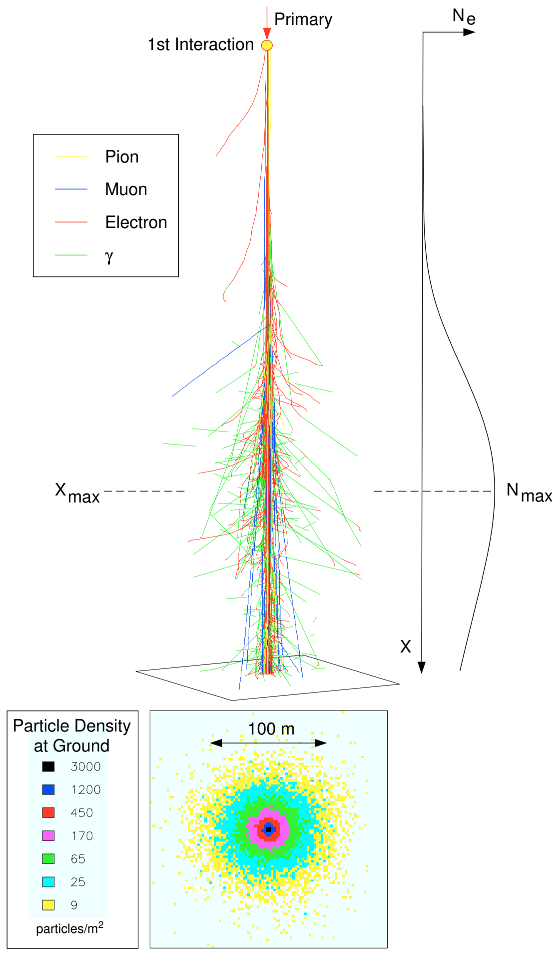

Figure 2.9: Different views on the development of an 1 PeV proton induced air shower (Hinton 1998).

Chapter 3

Experimental Setup

The L3 detector (L3 Collaboration 1990) was one of the four experiments at the Large Electron Positron collider (LEP) located at the European Organization for Nuclear Research (CERN). L3 was built with a special emphasis on detecting new particles, as the top quark had yet to be discovered and the Higgs particle still hasn't been observed. Therefore, it had been designed with a remarkably precise muon detector (MUCH), as compared to the other LEP detectors. After its completion it was proposed (Bähr *et al.* 1996) to use the exceptional size and resolution of this sub-detector to study cosmic ray muons. In 1998 a dedicated data acquisition system has been added to a part of the muon detector. A set of precise timing detectors consisting of scintillator modules was added as well. The setup was extended in 1999 to readout the complete MUCH, and additional time-zero counters were placed. In 2000 the setup was extended to its final form with the installation of a small Air Shower Array on the roof of the main hall above the L3 detector. It is the data taken with the final setup which is discussed in this work.

3.1 Geographical location

The L3+C detector was geographically located at longitude $6°01'17''$ and latitude $46°15'06''$ in France near Geneva, Switzerland. The surface altitude above sea level at the detector was 449 m. The detector itself was placed in a large experimental hall underground. The depth of the detector below the surface measured at the vertex point was 44.78 m. The accelerator plane was inclined by 1.39 % with respect to horizontal. The rock surrounding the experimental hall had been well studied for civil engineering

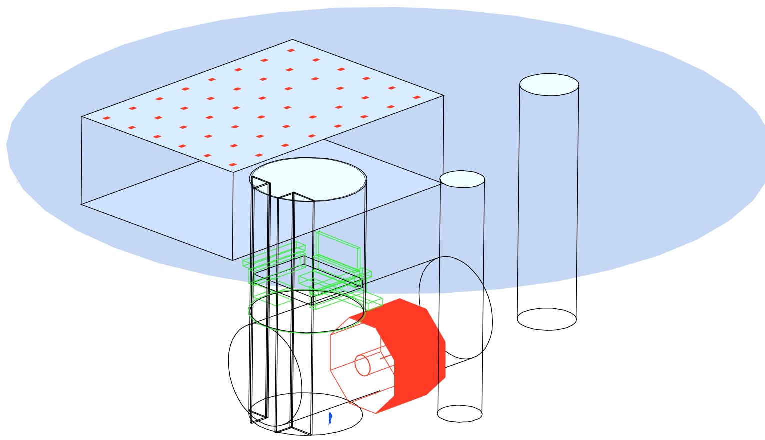

Figure 3.1: The L3 experiment and the Air Shower Array.

purposes and the results have been used to establish a GEANT simulation model of the cavern. Three shafts give access to the experimental hall. A large construction hall covers the main shaft and housed the electronics and facilities needed to operate the detector. Figure 3.1 shows the relative position of the L3 detector, the access shafts, the experimental hall, and the Air Shower Array installed on top of the construction hall.

3.2 The Muon Detector

This section briefly describes the muon system used in the L3+C experiment. A very detailed description of the muon detector, the readout electronics and monitoring software can be found in (Petersen 2002).

3.2.1 The magnet system

The L3 muon chambers were located inside an octagonal-based prism shaped solenoid, with a nominal field value of 0.51 T. The coil of the solenoid consists out of 168 wind-

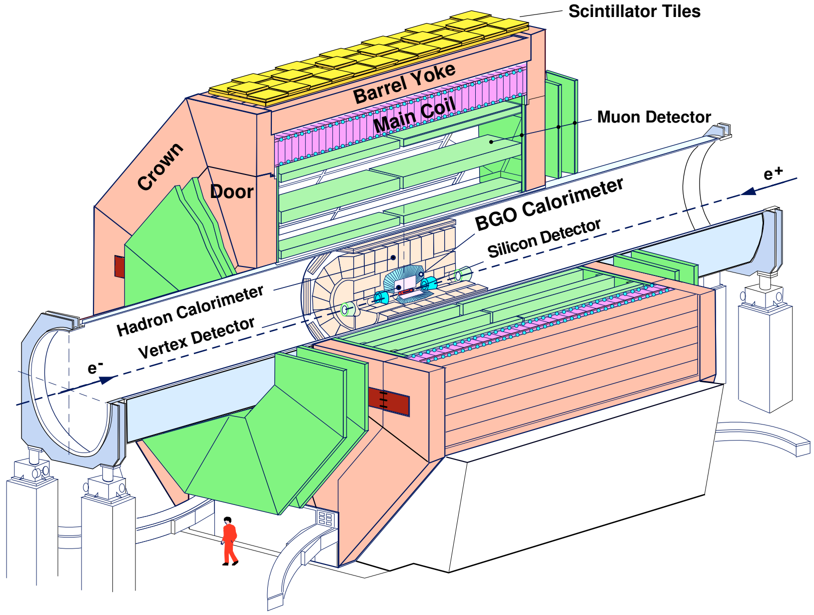

Figure 3.2: The L3 detector.

ings of water cooled aluminium conductor. This coil is enclosed in a iron frame acting as a return yoke of 14.1 m long, a thickness of 76.5 cm and a inner radius of 7.035 m. This iron cage is closed by a set of four doors, two at each end. A large stainless steal tube ran through the solenoid. The muon chambers were attached to the outside of this tube, the other L3 sub-detectors were located inside this tube. The L3+C time zero counters were positioned on the three top faces of the return yoke. A schematic overview L3 detector is given in figure 3.2. The magnetic field strength was monitored between the muon chambers by a set of about thousand magneto-resistors (Brouwer *et al.* 1992). In addition five nuclear magnetic resonance probes monitored the absolute value of the field. On the doors 36 windings provided a toroidal field of nominal value 1.24 T, as described in (L3 F/B Muon Group 1996).

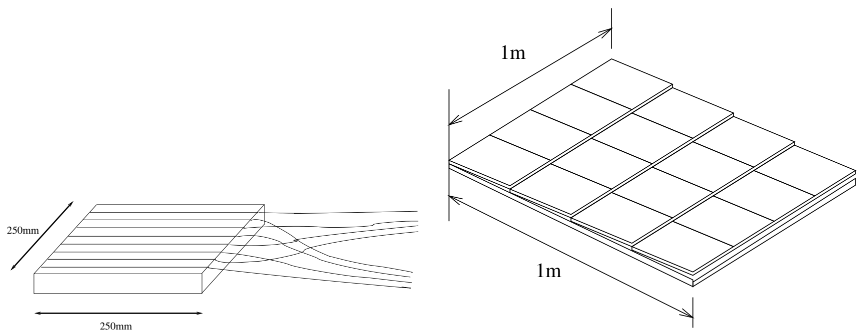

(a) A scintillator tile

(b) A cassette build out of 16 tiles

Figure 3.3: Details of the scintillator system.

3.2.2 The time zero counters

A total of 202 m^2 of scintillation detector had been added to the L3 setup for the timing of cosmic ray muons. The technology used is described in (Bähr *et al.* 1997). The detectors were distributed on the top three octants, with 72 m^2, 72 m^2, and 58 m^2 on octants 1, 2 and 3 respectively. The basic element is a $250\times 250\times 20$ mm^3 tile of scintillation plastic (figure 3.3a). In the upper surface eight 300 mm wavelength shifting fibres are glued into eight parallel grooves. One end of the fibre is coated with aluminium to reduce light losses. The other side is connected to 1800 mm plain fibres. The fibres of one tile are divided into two groups, each going to a photomultiplier, together with fibres originating from other tiles. Sixteen tiles form a 1 m^2 cassette (figure 3.3b). Six cassettes form a module. All tiles from a module are read out by the same two photomultipliers. The module formed the basic element from the read out point of view. The signals from the photomultipliers have to be above a given threshold. Afterwards a hit is formed by the coincidence (within 300 ns) of the signals from the two photomultipliers, to reduce photomultiplier noise. This reduced the rate on a single photomultiplier from about 60 kHz to a 2 kHz coincidence rate per module. The time information of both photomultipliers is recorded for later use in the offline reconstruction. The time of the earliest signal of a hit is used as time reference, because it is most likely to come from the photomultiplier having received the largest signal, and thus having the best time resolution.

3.2.3 The Muon drift chambers

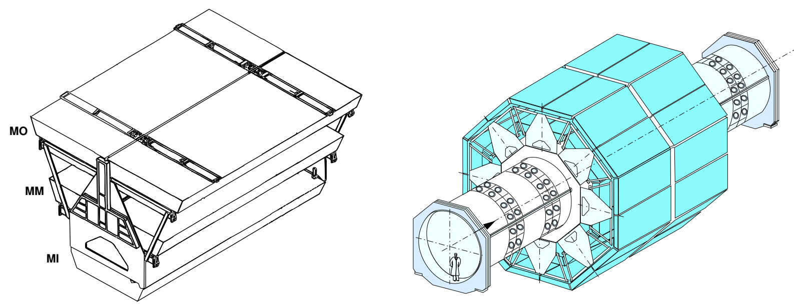

(a) An octant, composed of five drift chambers, assembled in three layers.

(b) Sixteen octants arranged in two Ferris wheels on the support tube

Figure 3.4: The central muon system.

The muon chambers are assembled on two *Ferris wheels*, labelled Master and Slave, each supported by the support tube. Each Ferris wheel carries eight *octants*. An octant consists of three layers of drift chambers, assembled on two A-frames. The drift chambers are of two kinds:

- *P-chambers* measure particle coordinates in the magnetic bending plane.
- *Z-chambers* measure particle coordinates in the direction parallel to the magnetic field lines.

The inner layer consists of a P-chamber (called MI) which is sandwiched in between two Z-chambers (called II and IM), one on the bottom of MI, the other on its top. The middle layer consist of two P-chambers (called MM), a left and a right one, but no Z-chambers. The outer layer consists of two P-chambers (MO), again one the left side, the other on the right side, each sandwiched between two Z-chambers (OM and OO).

The P-chambers

The combined measurement of a particle trajectory in the three P-layers allows one to determine the momentum of particles by measuring the curvature of their path. P-

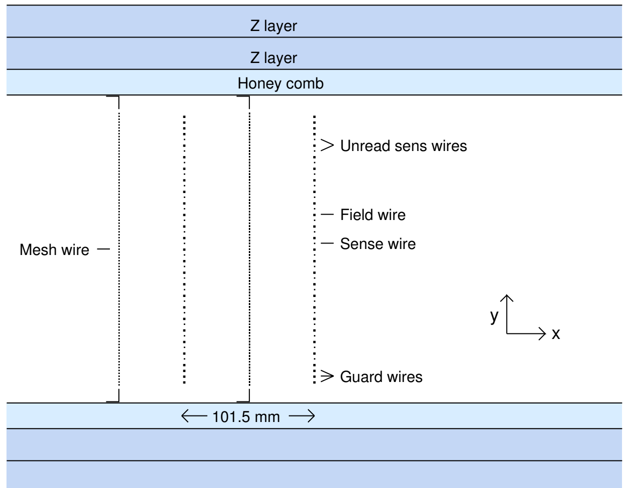

Figure 3.5: Detail of the MI/MO P-chamber.

chambers are built out of many 5.6 m long wires, accurately positioned by three Pyrex and carbon fibre bridges at the two extremities and in the middle, to reduce the gravitational sag of the wires to 95 µm. The logical unit formed by a group of wires is called a cell (see figure 3.5). Each cell consists of a cathode plane of *Mesh* wires vertically spaced at 2.25 mm from each other. Horizontally, at 50.75 mm from the cathode plane, is the anode plane toward which the free electrons drift. The sense wires on that plane are spaced by 9 mm. A field wire is located in between each pair of sense wires. The anode plane is extended at the bottom and at the top by a set of two sense wires which are in fact not read out, and four guard-wires, ensuring the homogeneity of the electric field for the outer sense wires. The MM chamber contains 24 active sense wires, whereas the MI and MO chambers only count 16. The gas mixture in the P-chambers is 61.5 % Argon and 38.5 % Methane. The high voltage settings and monitoring system are described in (Timmermans 1992).

A set of alignment systems called RASNIK consisting of LEDs at one end, a lens in the middle, and a 4 quadrant diode on the other side, monitor the position change of the MM chamber relative to the MI and MO chambers. Another RASNIK system monitors the position of the central bridges relative to the outer ones. The precision of this alignment system is of order 10 µm in the bending plane. A detailed description of the RASNIK system can be found in (Leijtens 1993).

The Z-chambers

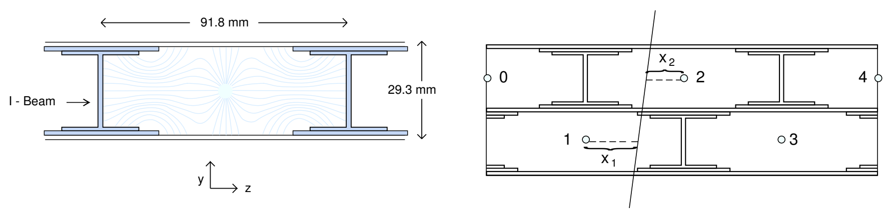

(a) A Z-cell, and the electric field lines

(b) Detail of a Z layer

Figure 3.6: Details of the Z-chambers.

The Z-chambers consist of two layers of rectangular drift cells. The I-beam (see figure 3.6a) acts as the cathode. The anode wire is located at the centre of the tube. The cells of the two layers are shifted by half a cell (see figure 3.6b). The gas mixture is 91.5 % Argon, 8.5 % Methane.

3.3 Dedicated readout

In order to be completely independent of the L_3 data acquisition (DAQ), which triggers only in coincidence with the LEP beams, an independent DAQ system has been added to the MUCH DAQ. This allows L_3+C to take data, independently of the state of L_3, as long as the magnet is on, and the MUCH is at nominal gas and high voltage settings. An overview of the readout hardware and its connectivity can be found in figure 3.7.

Access to the MUCH signals was realised by replacing the Muon Personality Card, preparing the signals for the L3-muon trigger, with a new card, the Cosmic Personality Card (CPC)(Groenstege, Wijnen, Rewiersma & Stolte 1999b). A part of the CPC reproduces the functionality of the former MPC card, another part contains three 32-channel time to digital converter (TDC) chips (Christiansen 1997) to measure the signal times, and logic preparing input signals (Majority signals) for the Cosmic Trigger and Timer (CTT) (Verkooijen 1999). The majority signal is sent when the number of input channels with signal reach a given threshold. The majority signals from a single

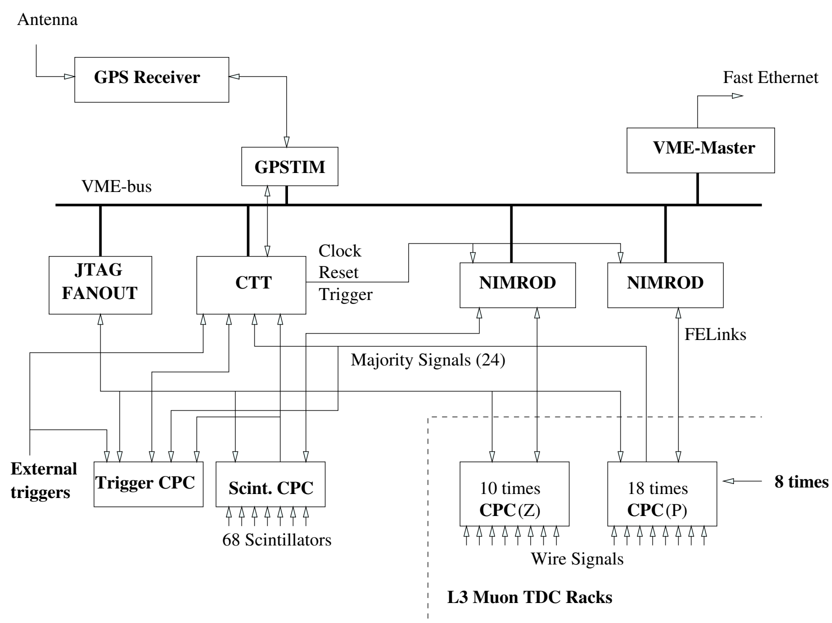

Figure 3.7: Overview of the readout system.

muon layer (MI, MM or MO) within an octant are OR-ed, so the CTT receives 24 Majority signals (3 layers × 8 octants). The majority logic is not used on CPCs connected to the Z-chambers, which do not contribute to the trigger.

The CPCs are read out by the NIMROD modules (Groenstege, Rewiersma, Wijnen & Zwart 1999a). A NIMROD is essentially an event building module, it receives the data from up to 16 CPCs, and stores it in FIFOs. The data from each event are combined into the central memory. When events are complete, they are readout from the memory via a VME bus. A MVME2600 Power-PC reads out all the NIMRODs and processes the final event building. The NIMROD provides the CPC with 10 MHz and 40 MHz clock signals, and provides the CPC with the trigger signal issued by the CTT. When the load on one NIMROD becomes too large it is able to instruct the CTT to hold off the triggers until it is able to process again. The CTT itself will impose a 4 μs dead time to avoid overlapping events, which is essentially the only deadtime of the data acquisition. It would also hold off the triggers when too many events have not yet been read out by the Power-PC.

The CTT module receives the majority signals and a signal from the scintillators-CPC, formed by the OR of all scintillator signals. When a suitable pattern is found on these inputs, it issues a trigger to the NIMRODs as well as to the GPSTIM (Leich 1998). The GPSTIM module prepares the clock signals, being itself synchronised to a GPS receiver. It keeps track of the time since the start of a run, it also measures the livetime by counting the clock cycles whenever the experiment is open for triggers, and provides a time stamp to each event.

It is to notice that the clock of the GPS receiver had a problem in the second counter. This counter may show a 7 to 11 seconds jump forward in time. Within a minute, this would be reset as the receiver readjusts its time to the signal provided by the satellites. About 5% of the runs taken with the MUCH detector were affected by this, and the concerned runs used in this work were manually corrected.

3.4 The Air-Shower array

3.4.1 Detectors

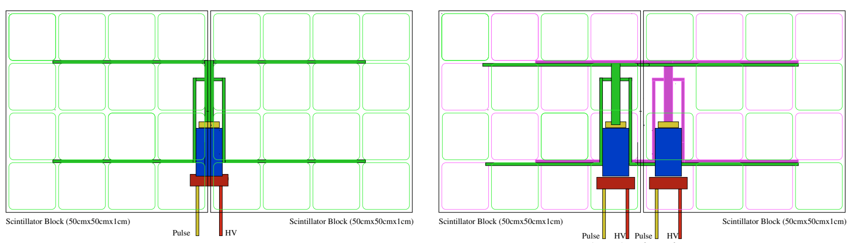

(a) Module with one PMT (b) Module with two PMTs

Figure 3.8: The two types of Air Shower Array scintillator modules.

The L3+C Air Shower Array consists of 47 scintillator modules, arranged in six rows of eight modules, as shown in figure 3.1, and located on the $60{\times}35\,\mathrm{m}^2$ roof of the SX-hall. The module which would have been in the third position on the third row is missing since the slant cover to the main access shaft prevents the module from being positioned there. A module consists of two pieces of plastic of dimensions $50{\times}50{\times}1\,\mathrm{cm}^3$. On the upper surface of each piece, 16 σ-shaped grooves are filled with wavelength-shifting fibres. The 32 fibres bring the collected photons to a photomultiplier, as can be seen in figure 3.8. The plastic and the photomultiplier are enclosed in a light tight aluminium box. An additional cover protects the module from solar radiation, rain, and snow.

3.4.2 Air Shower readout

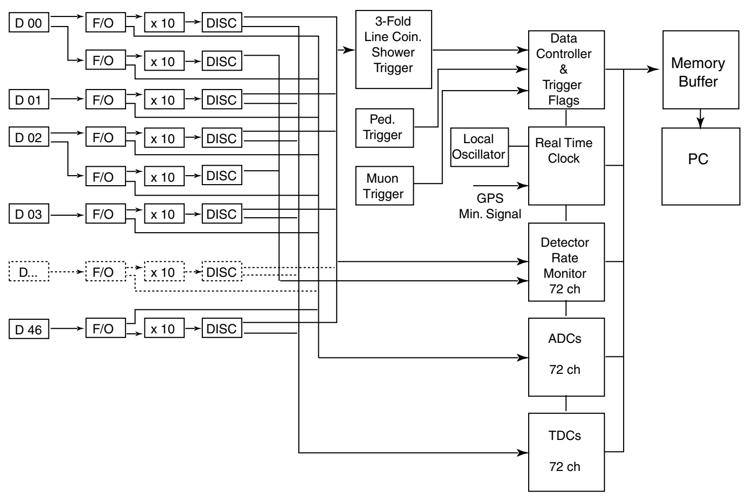

Figure 3.9: Air Shower Array DAQ layout.

A dedicated readout was built around a custom made trigger logic. The signals from the photomultipliers are split into two. One part passes an amplifier and a discriminator, and is used as input for the trigger and the TDCs (Lecroy 2228). The other part is fed to the analogue to digital converter (ADC) (Lecroy 2249 A). When the trigger fires, both the photomultiplier pulse height and signal time are recorded. There are two types of triggers: The shower trigger requires at least one module with a signal above threshold in each of three adjacent rows. The pedestal trigger uses the signal of a local oscillator to fire every 10 seconds. It also uses the GPS signal to fire every minute. Figure 3.9 shows how detectors D00 to D46 are connected to the trigger.

The dynamic range of the measurements is of primordial importance to correctly estimate the number of particles in large showers. For this purpose 12 of the detectors are equipped with a second photomultiplier operated at a lower gain. The 32 fibres are then distributed alternatively to the two photomultipliers. The signal from the low gain photomultiplier does not participate to the trigger decision, and its time information is not recorded. These are for instance D00 and D02 on Figure 3.9.

The Air Shower Array detector and the muon detector are connected by exchange of the trigger signals. When a trigger takes place in one of the detectors, a signal is sent to the other. If that detector had a trigger as well, the signal gets recorded in its data. This is of course not enough to match events unambiguously as there may be noise or inefficiencies on the trigger exchange lines. In addition, the time stamps of the events have to be compared. Since the time stamps are taken from local clocks at each sub-detector, the difference can be time-dependent. In the first period of data taking the Air Shower clock was synchronised only once with the GPS, and the time differences fluctuate in time. After August 7, synchronisation was more frequent and the time difference remains constant. At the end, the time correlation is lost and only present during very short periods of a few minutes.

3.4.3 Air Shower Array calibration

To use the information recorded by the array, the response of each ADC-channel has to be known for a minimum ionising particle (MIP) . Each day one of the channels was disconnected from the array DAQ system. This channel was then connected to a special ADC via an amplifier of gain 10. The trigger for this ADC was generated by a small telescope consisting of two $20\times20\,\text{cm}^2$ scintillation counters. The coincidence of these two counters generate the calibration trigger. The telescope was placed on top of the protective cover of the Air Shower Array module being calibrated. As an example Figure 3.10 shows the recorded charge distribution in the case of ADC channel 59.

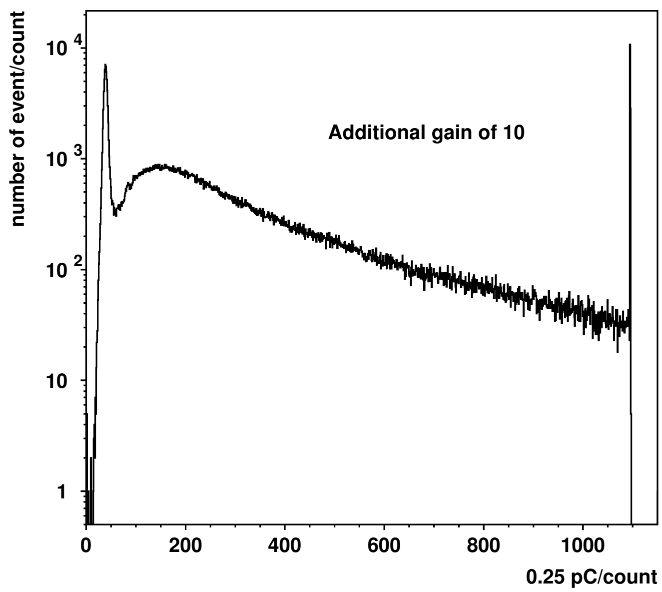

Figure 3.10: Calibration measurement of ADC channel 59.

Chapter 4

Reconstructing air showers

This chapter explains how to extract useful parameters from the signals recorded in the Air Shower Array. The available information consists of the arrival times of the pulses with respect to the trigger decision, and the total charge carried by these pulses. The parameters which can be extracted from this information are the direction of the shower, using the timing information, and the shower core position, size and shape (also referred to as age), using the collected charge information.

4.1 Shower direction reconstruction

The directional information is reconstructed using the timing information of the scintillator signals. The particles come in as a flat pancake perpendicular to the shower direction. The curvature of the shower front is negligible due to the small size of the array, the effect being of the order of 1 ns at a typical distance of 25 m (KASCADE Collaboration 2001c).

The estimation procedure compares the measured arrival time t_i, and its estimated error σ_i, of module i at position (x_i, y_i) with the predicted arrival time of a given shower direction using a χ^2:

$$\chi^2 = \sum_i \frac{(t_i - t_0 - ax_i - by_i)^2}{\sigma_i^2} \tag{4.1}$$

The shower direction in polar coordinates (θ, ϕ) is related to a and b in the following way:

$$\theta = \sin^{-1}\left(c\sqrt{a^2+b^2}\right) \tag{4.2}$$

$$\phi = \tan^{-1}\left(\frac{b}{a}\right) \tag{4.3}$$

A closed solution for this χ^2 minimisation problem exists and determines the angles (θ, ϕ). Adding an element of the kernel of the $d\chi^2$ form to the times changes the value of the parameters a and b, but not the minimum value of the χ^2. This means one can choose a set of time corrections $t_i^c = \delta a x_i + \delta b y_i$ which modifies the estimated parameter a and b into $a + \delta a$ and $b + \delta b$. A set of corrections was chosen such that on average the shower direction and the muon direction as measured in the L3+C muon spectrometer coincide.

4.1.1 Delay correction

The timing of the scintillator signals is digitised by Lecroy TDC-2228 TDC running at 500 ps per count. From the photomultiplier to the TDC the signals travel over 100 m of coaxial cable, through an amplifier and a discriminator, and over 80 m of delay line. This introduces relative delays between each of the channels, which need to be corrected for.

The correction constants are extracted from the mean of the residuals of the time fit for each module. The procedure is iterated until all residuals are close to zero, within about 100 ps.

module	0	1	2	3	4	5	6	7
row 0	3.35	12.48	-1.90	-2.65	-1.55	5.85	0.66	3.97
row 1	-1.06	-4.63	5.99	11.47	7.39	2.98	-0.96	13.06
row 2	0.79	-1.27		-6.50	0.08	1.41	-2.58	-6.82
row 3	-7.91	-4.34	-6.26	-11.57	-14.46	-9.89	0.79	-5.17
row 4	-2.20	-5.48	0.15	-11.06	-9.60	-2.85	1.66	-1.81
row 5	-4.98	-0.60	-4.78	10.14	-6.42	-6.94	-13.26	-9.07

Table 4.1: Time corrections for each module in ns

4.1.2 Time slewing correction

Large signals from the modules fire the discriminator earlier than small signals do. This is taken into account by the time slewing correction. The time slewing correction was measured from the mean residual as function of the collected charge readouts. It has been parametrised in the following way: $t_{slew}(Q) = \frac{P_1}{(Q+P_2)^2} + P_3$ns. Q is the pedestal subtracted ADC readout, parameters P_1, P_2 and P_3 are estimated for each channel. An example is shown in Figure 4.1a. The function does not completely describe the data, hence the bad quality of fit. However the discrepancies are of order 100 ps, which has to be compared to the uncertainty on a single measurement, which is of order several nanosecondes as will be shown in next subsection.

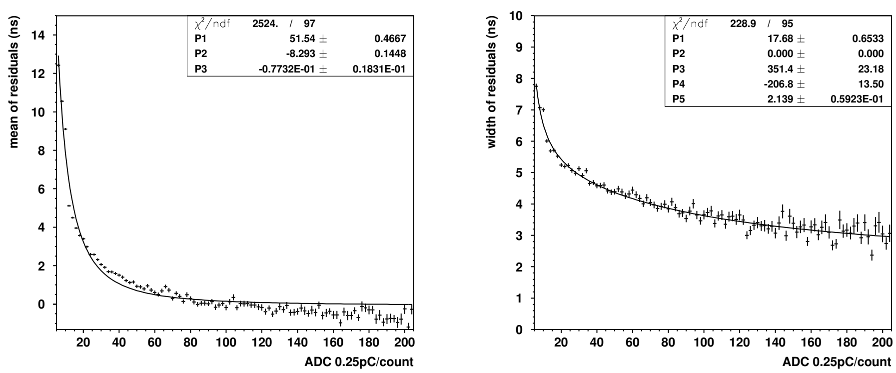

(a) Estimated time slewing function and data.

(b) Estimated resolution function and data.

Figure 4.1: From the residual distributions it is possible to extract the time slewing correction using the mean value of a Gaussian fitted to the distribution (a), as well a the time resolution using the standard deviation of that same Gaussian (b). Module 4 was chosen for this illustration.

4.1.3 Errors on the time measurement

The expected error σ_i on each time measurement also depends on the collected charge. For large signals, there is a sharp raising edge. The time that the signal reaches the threshold of the discriminator is therefore better determined. The estimator on the error on the time measurement is extracted from the standard deviation of the residual distribution. It has been parametrised as $\sigma(Q) = P_5 + \frac{P_1}{Q+P_2} + \left(\frac{P_3}{Q+P_4}\right)^2$ ns, for all modules. These parameters are estimated for each channel, except P_2 which is fixed at 0. An example is shown in Figure 4.1b

4.1.4 Cuts against electronic noise

Some channels show random triggers, with TDC readouts higher than 300 ns. Normal readouts are centred around a readout value of 100 ns. All readouts above 300 ns are ignored. Sometimes TDC channels fire when the ADC readout is below the pedestal value. These TDC readouts are also ignored. At least 9 modules should have a good TDC readout for the first fit to be performed. The fit is then repeated dropping all hits having a residual of more than five times the estimated error.

4.2 Shower size estimation

When observing Air Showers, one of the interesting quantities is the energy of the particle involved in the first interaction. Air Shower arrays function as a very simple calorimeter using the atmosphere as an absorber, and consisting of only one single sampling plane, at the rear end of the absorber. The principle is as any calorimeter, to measure particle multiplicities which have something to do with the amount of energy that was available for the particle creation. The true information delivered by the detector system is not directly the number of particles but the total amount of charge generated by the photomultipliers when particles cross the scintillation modules. This section describes the procedure used to build an estimator for the primary energy. It will be called shower size and in reality is closer to an estimator of the total number of charged particles on the sampling plane.

4.2.1 Pedestal measurements

For each run the pedestals are measured from unbiased triggers. Every 10 seconds the trigger is fired by the local clock, each minute the trigger is fired by the GPS minute signal. These triggers provide the pedestal values, as shown in figure 4.2.

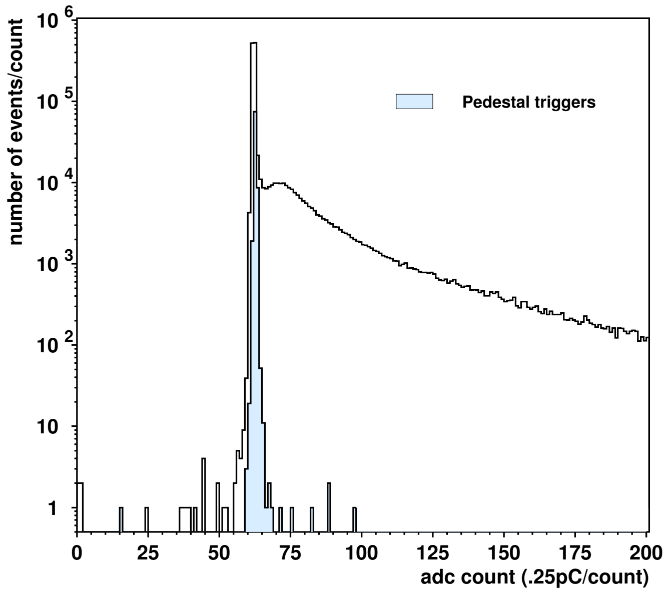

Figure 4.2: Collected charge distribution for channel 59. The hatched area corresponds to the collected charge for the pedestal triggers.

4.2.2 Fit procedure

It is assumed that the function of Nishimura, Kamata (Kamata & Nishimura 1958), modified by Greisen (Greisen 1960) (NKG function) is well suited to describe the charged particle lateral distributions in air showers. Other descriptions of the density distribution as described in (Lagutin, Plyasheshnikov & Goncharov 1998), and in (Capdevielle *et al.* 2001) are not used in this work. Let $\rho(r)$ be the particle density at a distance r from the shower axis:

$$\rho(r) = \frac{Ne}{r_M^2} \frac{\Gamma(4.5 - s)}{2\pi\Gamma(s)\Gamma(4.5 - 2s)} (\frac{r}{r_M})^{s-2} (1 + \frac{r}{r_M})^{s-4.5} \quad (4.4)$$

The Euler Γ-functions are included for normalisation. Ne is the total number of particles, r_M is the Molière radius. r is the distance to the shower core, at which the density $\rho(r)$ is estimated. Finally, s is called the age parameter, and fixes the shape of the distribution. At young ages (s=0.0), the density is sharply peaked at the core. At large ages (s=2.0) the density is very flat. Intuitively speaking old showers started high up in the atmosphere, and many particles diffused laterally to larger distances from the shower axis. In young showers most particles are still in the shower core.

In the NKG function the Molière radius is replaced by r_{eff} =35 m, an effective radius, close to the typical distances within the Air Shower Array. This is possible as changes in r_{eff} can essentially be compensated for, by changes in s. This is suggested by the studies of the KASCADE collaboration (KASCADE Collaboration 2001b).

The fit is only performed when a direction has been found for the shower, and when the total number of modules with a MIP count larger than 3 exceeds 10, which reduces the amount of computer time spent on very small showers, with no clean core. The fit procedure searches for a maximum of the likelihood L of observing the measured data Q_m, varying the shower core position, the total number of charged particles Ne, and the age parameter s, using MINUIT (James 1994) to minimise:

$$\begin{aligned} -\ln L = -\sum_{channels} \ln\Big(& P(Q_m|0)P(0|\rho_m) \\ & + (1-\epsilon_m)P(n>0|\rho_m) \\ & + \epsilon_m \sum_{n>0} P(Q_m|n)P(n|\rho_m)\Big) \end{aligned} \tag{4.5}$$

Assuming a core position, and using the previously determined shower direction, the distance of each module to the shower axis can be calculated, and integrating equation 4.4 over the size of the module seen along the shower axis, the expected number of particles ρ_m is obtained. ϵ_m is the efficiency of the module. $P(n|\rho_m)$ is the Poisson probability of observing n particles while expecting ρ_m. $P(\mathrm{Q}|n)$ is assigned according to the following three cases:

- $P(\mathrm{Q}|0)$ is the probability of observing Q from a fluctuation of the pedestal value. Here a gaussian distribution is used centered on the measured mean pedestal value, and the rms of the measured pedestal distribution as its standard deviation.

- For $n > 0$ and the module not being saturated, $P(\mathrm{Q}|n)$ is the estimation of the probability of measuring the observed value Q, assuming that n MIPs crossed the scintillation counter. These probabilities are estimated using the calibration

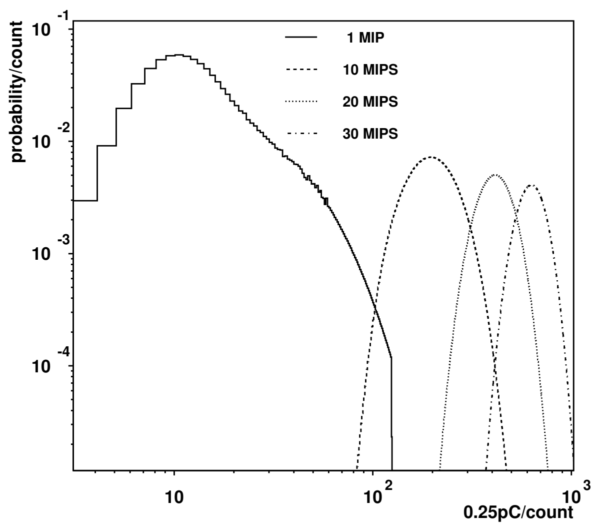

Figure 4.3: Predicted ADC probability distributions for 1, 10, 20 and 30 MIPs, for module 0.

measurements for one MIP, and convolving it n times for the probability of observing n. See figure 4.3.

- For $n > 0$ and the module being saturated, $P(\mathrm{Q}|n)$ is the estimation of the probability of measuring any count larger than the ADC count at saturation. These probabilities are calculated from the unsaturated probabilities.

Figure 4.4 shows such a reconstructed event, displaying the measured quantities and the estimated quantities.

ADC efficiencies

The efficiency of each channel can be estimated using its neighbours. When surrounding modules record large signals, the module in study is also expected to have a readout above the pedestal. For this estimation it was required that a channel had at least two

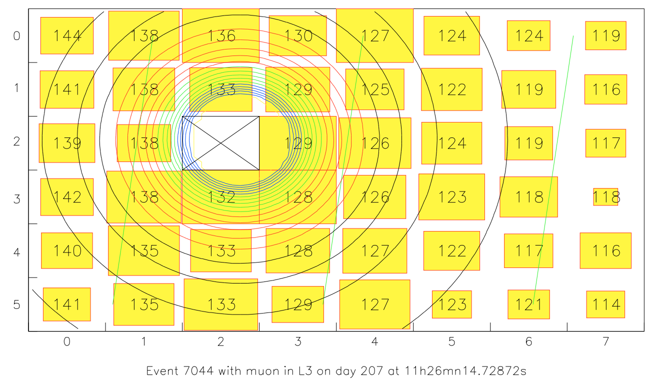

Figure 4.4: Example of a recontructed AS event. The surface of the rectangles is proportional to the ADC signals, the numbers indicated on each module are the arrival times ot the signals. The contours indicate the estimated NKG distribution, and the three lines indicate lines of equal arrival times.

adjacent channels connected, and that the average collected charge was larger than 27 pC, (of order 10 MIP equivalents). The time stability of these efficiencies have been checked to be stable within the accuracy of the method. Notice that this accuracy is of order 3 % when taking all data from 10 days together. The measured efficiencies are shown in table 4.2. Scintillation modules readout by two photomultipliers have two entries in this table. It is to notice that for these modules the two measured efficiencies are very close. This suggest that the main source of inefficiency can be assigned to the quality of the used plastic.

Electronic noise suppression

For each run, typically 7748 events, the ADC spectra of each channel is compared to a reference distribution. When the difference between the two distributions is too big, that is if the reduced χ^2 is larger than 1.5, the channel is assumed to be disconnected for that run. The disconnected channels are excluded from the fitting procedure. This method ensures that the channel disconnected for calibration as described in section 3.4.3 is not used. Also, it rejects channels which are temporary malfunctioning or have high noise.

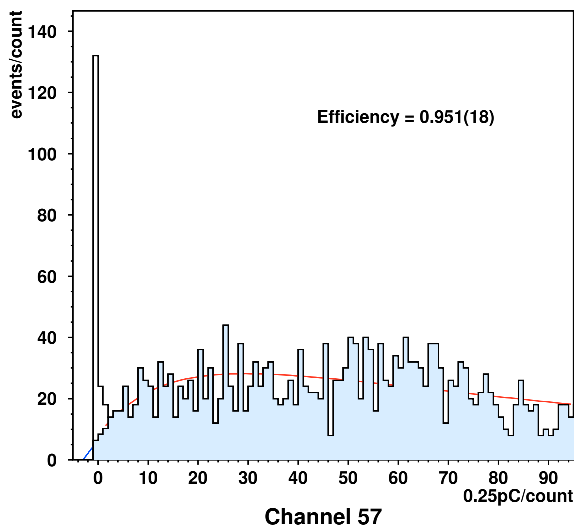

Figure 4.5: ADC spectra for channel 57, for high neighbouring signals. Also shown is the estimated efficient signals as the hatched area.

4.3 Muon counting

Counting muons in the MUCH detector was not satisfactory in the standard reconstruction described for instance in (Petersen 2002). In this program the reconstruction of tracks is performed within an octant, thus it limits the number of reconstructed tracks. This choice was motivated by the historical legacy of the L_3 software, and that this program was only designed for the measurement of the muon spectrum, therefore concentrates on the high quality tracks which is only achievable within an octant. To get a idea, the final acceptance for these high quality tracks $0.14\,\mathrm{m}^2\mathrm{sr}$ for tracks within $10°$ from vertical.

Two independent counting methods have been developed. The first one is based on the raw-data, and has been developed by C. Timmermans. This methods first tries to estimate the number of muons crossing each P-cell. Afterwards, the direction of

	module 0	module 1	module 2	module 3	module 4	module 5	module 6	module 7
row 0	0.945(10) 0.940(10)	0.976(11)	0.969(11) 0.965(11)	0.964(11)	0.961(9) 0.976(9)	0.958(9)	0.966(10) 0.971(10)	0.910(9)
row 1	0.965(10)	0.966(11)	0.966(11)	0.972(10)	0.971(11)	0.959(10)	0.969(10)	0.953(8)
row 2	0.952(9)	0.965(10)		0.965(10) 0.966(12)	0.970(9)	0.958(9)	0.969(9)	0.955(9) 0.955(9)
row 3	0.961(8)	0.962(9) 0.961(9)	0.969(9)	0.968(9)	0.963(9)	0.961(9) 0.960(9)	0.956(8)	0.946(8)
row 4	0.961(9)	0.964(9)	0.964(9)	0.958(8)	0.955(8)	0.965(9)	0.966(8)	0.955(8)
row 5	0.933(8) 0.942(8)	0.958(8)	0.964(8) 0.959(8)	0.953(9)	0.954(8) 0.947(8)	0.952(8)	0.949(8) 0.939(7)	0.858(7)

Table 4.2: Estimated efficiencies for each of the ADC channel.

the incoming muons in the bending plane is determined, followed by a matching of muons from different cells on the bases of the angle. For each track at least two cells are required. This method will be referred to as CT counting (Timmermans 2001).

The second muon counting program, based on an original layout by the author, and all the credit goes to V. Schmitt and L. Lee for the implementation. Here a full scale pattern recognition is performed. Hits are grouped in each chamber in *segments*. This is performed by determining the distance to some reference point and angle with respect to vertical of all lines defined by hit pairs in a chamber [1]. Clusters in this two dimensional representation of a line are recognised as segments. Contrary to the original program where this was performed in a local based coordinate system, this is now done in a global system. Circles are fitted to the segments using the non iterative method described in (Karimäki 1991). Some clean up is performed rejecting segments which are covered by larger ones. Each segment is characterised by three quantities, it's curvature ρ, the distance of closest approach to the origin d, and the angle of the tangent to the circle at the point of closest approach with the horizontal direction Φ. The algorithm makes pairs of segments and keeps the pairs with good quality of fit. Clusters in the (ρ, d) plane are divided in *groups* of unambiguous segments sets. Each group contain many possible combinations of segments, all these combination are refitted, and the combination with the best quality of fit is kept, removing all direct ambiguities to it. The procedure is repeated with the remaining segment sets. Later Z-segments are added to the groups to form tracks and a swim fit is performed in a similar fashion as the original program. Yet in this work, considering the aged and noisy status of the Z-chambers after 11 years of operation without maintenance, the number of two dimensional groups is used as an estimator of the number of tracks. The technical details of the pattern recognition can be found in (Schmitt 2000). This counting method

[1] A hit pair defines four spatial points as their is an ambiguity about the real hit being in the left or right part of a cell, therefore defines four lines.

will be called XO counting.

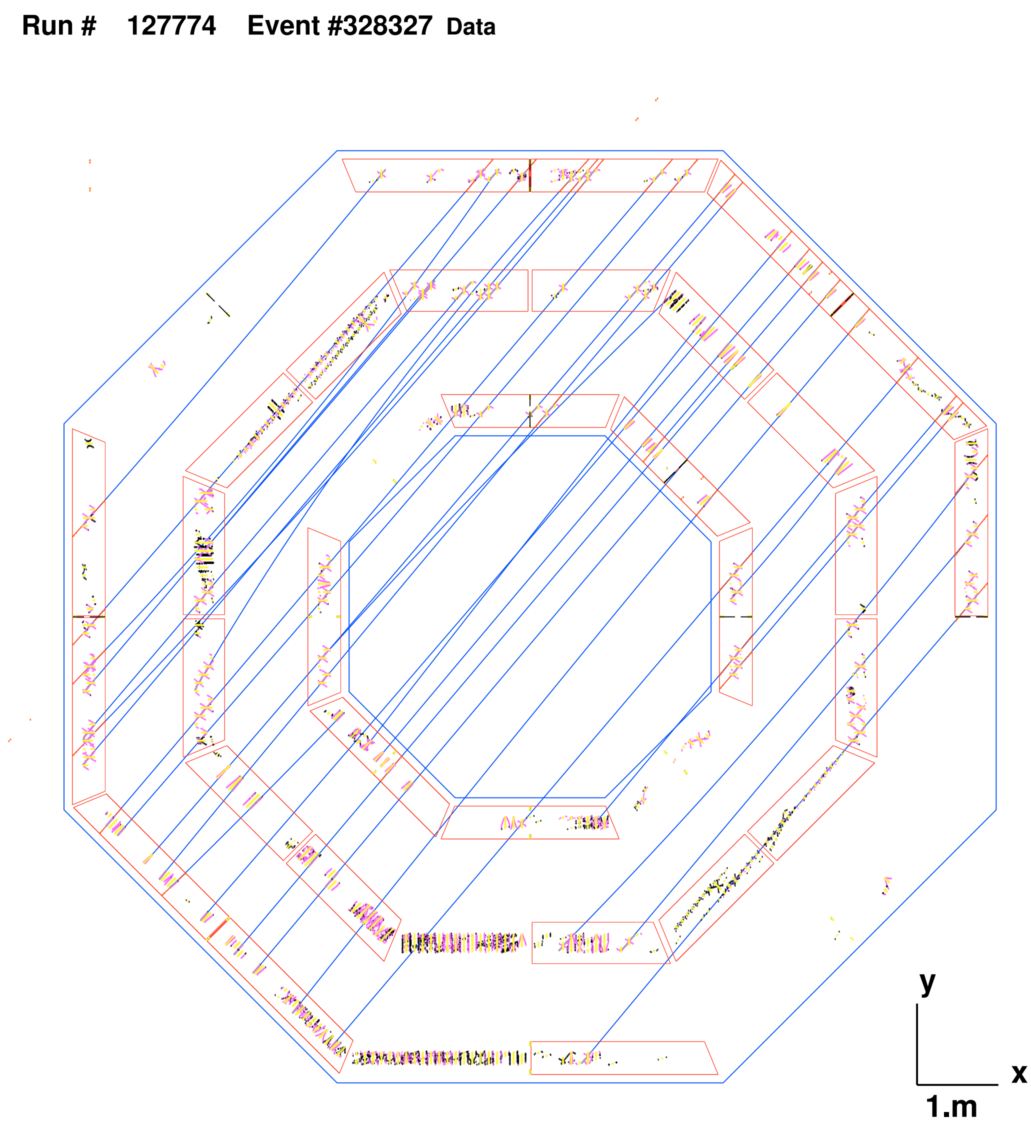

Figure 4.6: Example of an event reconstructed the XO program. The estimated multiplicity is 29 for this event.

Chapter 5

Selections

In this chapter the selections used in the following chapters will be reviewed. When Monte-Carlo is needed to investigate resolutions or efficiencies, systematically the proton simulations will be used as it is known that in the region of interest of this work, from about 50 TeV to 10 PeV, which is partly in reach of direct experiments, the composition is dominated by light ions as proton and helium. Also non observable quantities, known in the simulation, as the primary energy or the true core position, will never be used for selection, but only to compare to estimations.

5.1 Run selection

In this work, the data used are the events recorded by the Air shower array, at times when the muon detector was also operational. The period of data-taking period concerned was between June 11 2002 and August 29. The reason later data are not used is twofold. The time correlation between the two detectors was lost on August 30. A few days later some of the TDC s in the Air Shower Array started malfunctioning.

A total of 1,890,332 events were recorded during that period. From the MUCH data events with AS-trigger were extracted from the total sample to create a more manageable set. It is this subset which is matched with the AS data. Some MUCH events are lost this way, as inefficiencies may occur on the down trigger exchange line (from Air Shower Array to MUCH detector). Such inefficiencies appear as events which are flagged in the AS-data but have no matching counter part in the MUCH-data. This affects 3.46 % of the events, and are strongly fluctuating in time. The TDCs used in the readout of the muon system are known to have inefficiencies of this order.

The events without flag, but having a muon with flag in 0.1 ms time coincidence, amount to 0.15 %, and has to be assigned to inefficiency of the up trigger exchange line. These events will be considered as matched anyway.

The muon runs 110152 up to 110170 are excluded, as gas, high voltage and discriminator systems had major problems. An other set of muon runs have been excluded on the basis of their trigger rate. The normal trigger rate was either 418 Hz, or 426 Hz, as the trigger settings were slightly modified over the period. 53 runs, during the period of interest, with trigger rate below 400 Hz or above 700 Hz were rejected, these runs corresponds to the hatched areas on figure 5.1a.

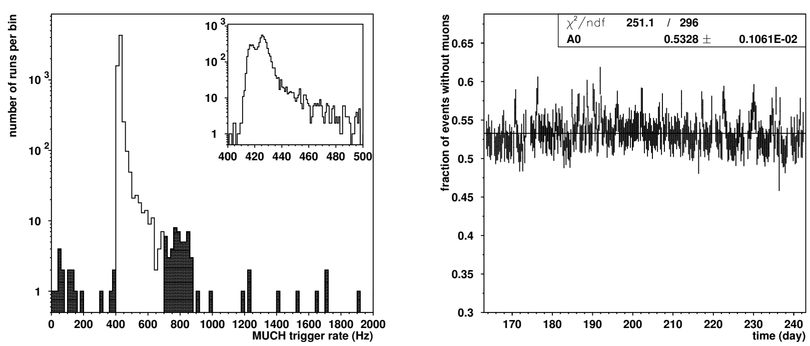

(a) Distribution of the trigger rate per run. The hatched areas correspond to the runs which are excluded from the analysis on the basis of their deviant rate.

(b) Time dependence of the fraction of events without muons. The errors shown are statistical and systematical

Figure 5.1: The MUCH trigger rate and the fraction of events without muon(s).

After these run selection the fraction of events without muons show the stability one expects. Figure 5.1b shows this fraction evaluated for each six hour period over the total time period. The estimated errors are the statistical fluctuations on a binomial distribution, and a systematic part describing the 3.46 % muon event loss weighted by the fraction of event with muons. One sees that this contribution slowly fluctuates in time.

5.2 Event selection

5.2.1 Selection on the shower direction

The acceptance of the MUCH detector has a very complicated shape, due to the presence of the access shafts, and the dead areas of the detector, where both the none instrumented regions as well as the inefficient regions contribute. Also it is known from (Petersen 2002) that despite the effort made by many to get the setup correctly described in GEANT, it is not perfect for muon energies close to the energy threshold imposed by the molasse. Therefore, limiting the analysis to showers as close to vertical as possible gives better control on the following points:

- The energy threshold for muons would depend less on position and direction.
- The acceptance of both the Air Shower Array and the MUCH detector would be less dependent on the azimuthal angle.

Table 5.1 shows the remaining fraction of data for different values of the cut on the zenith angle. Restraining the cosine of the zenith angle to a value as high as 0.9 might

Minimal cosine of zenith angle	0.6	0.65	0.7	0.75	0.8	0.85	0.9	0.95
Percentage of data	99.3	98.6	97.2	94.4	89.4	80.3	64.9	39.7

Table 5.1: Fraction of events above eight values of the cosine of the zenith angle.

seem acceptable from the values of the table. Yet it is in fact not. A very interesting feature of the setup is that the muon content of showers can be studied as a function of distance to the shower core. The restriction to only vertical showers would reduce the acceptance for showers with axes passing through the MUCH detector and for the showers at the largest distances from it. A cut off at 0.8 would seem reasonable from that point of view. Therefore the selected showers, taking both arguments into account, are limited in zenith angle to a cosine value greater than 0.85 (corresponding to 31.8°).

5.2.2 Selection on the shower core position

For a correct estimation of the size of a shower, it is important to have a good estimate of the position of the shower core position. Figure 5.2.2 shows the resolution on the two coordinates of the core position, as a function of its abscissa and ordinate. The resolution is extracted from the Monte Carlo, estimating the width of a Gaussian, fitted to the distribution of the differences between real and estimated coordinates. The real

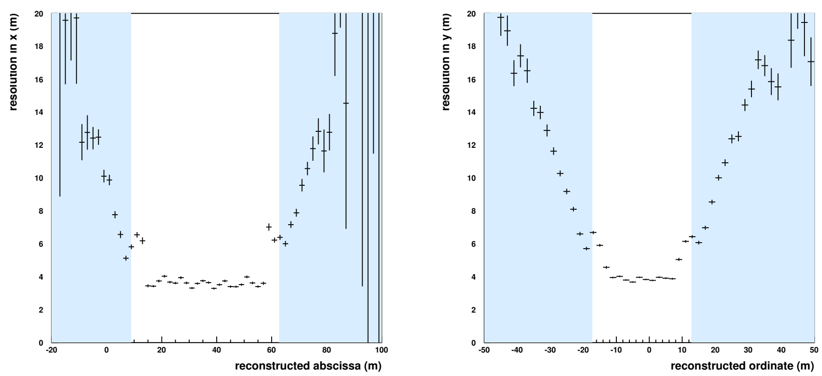

(a) Resolution on the shower abscissa, estimate from the width of a Gaussian fit to the difference between the true and the reconstructed core abscissa. The true ordinate is required to be within 10 m of the origin.

(b) Resolution on the shower ordinate, estimated from the width of a Gaussian fit to the difference between the true and the reconstructed core ordinate. The true abscissa is required to be within 30 m of the origin.

Figure 5.2: Resolution on the estimated shower core position from proton induced showers, all models were used.

core position is known from the generation of the shower, the estimation of the core coordinates from reconstructing the shower after the detector simulation. Two lines indicate the positions of the outermost scintillation modules. The shaded areas show the excluded regions on the base of this selection. The previously discussed selection is included in this figure.

This selection may at this stage seem too lose, as the resolution already starts deteriorating at 3 m from the boundaries. But a selection will be described in the next subsection which improves the resolution and make all the events reconstructed inside of the array usable.

The small oscillation observed in the resolution inside the array is explained by the preference of the fitting procedure to estimate the shower core position centred on a scintillation module.

5.2.3 Selection on the shower age parameter

The shower age parameter described in section 4.2, is essentially a shape parameter. At small ages the showers are sharply peaked, most particles being within one Moliere radius of the core position. At large ages the showers are flat and the core position gets more difficult to estimate, as can be seen in figure 5.3. This suggests that it is better to select events with small age. Yet when the number of measured particles increases one gets more sensitive to the shape changes. Such a cut on the age parameter should therefore be size dependent.

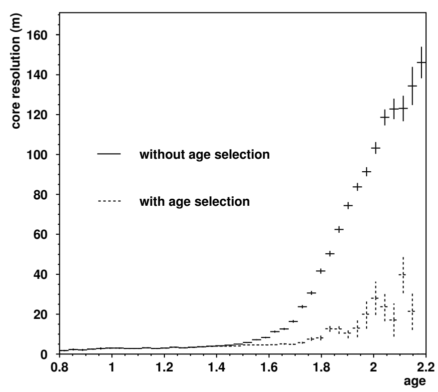

Figure 5.3: Resolution of the shower core as function of age, before and after the selection.

Figure 5.4 shows the proposed cut in the age and size plane. The background is shown the region in which the number of badly reconstructed showers, with estimated core position more than 5 m away from the true core position exceeds the number better reconstructed showers. It is noticeable that most of the unwanted region is above the cut line, and will be excluded. The improvement on the resolution can be seen in figure 5.3. At very high sizes, the scintillation counters saturate, inducing both a loss in position resolution, and a flattening of the shower shape. Therefore the cut was chosen so as to conserve these intrinsically interesting events. At very low sizes there is also a region of ill reconstructed showers below the cut line. These events will be taken care of by a cut on the number of modules with a signal present in the event. The justification of this new cut follows.

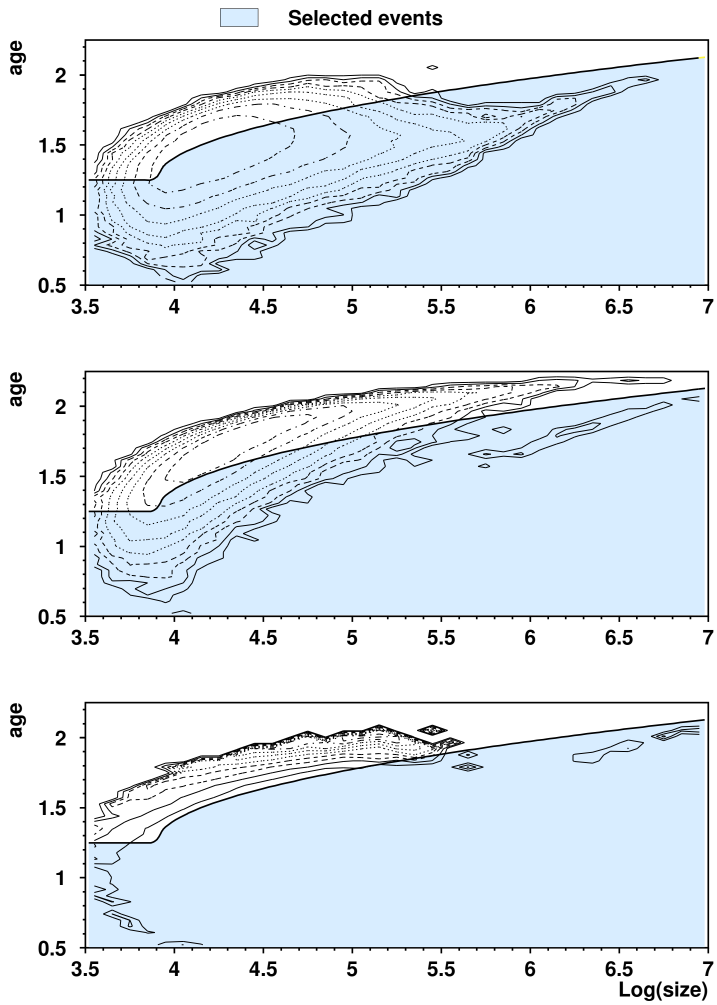

Figure 5.4: Top: distribution of the events in the (age,size) plane, for showers reconstructed within 5 m of their core position. Center: idem for shower reconstructed more than 5 m from their core position. Bottom: ratio of the two distributions only the region where the bad resolution showers exceeds the good resolution showers is shown. On all three plots the discussed selection is displayed.

5.2.4 Selection on the number of modules

The obtained size spectrum with the described selections shows for data lower numbers events of very small sizes (below $10^{4.3}$) than the predictions for proton, as shown on the upper part of figure 5.5 in the case of the QGSJET model, other models are similar but not shown for the legibility of the figure.

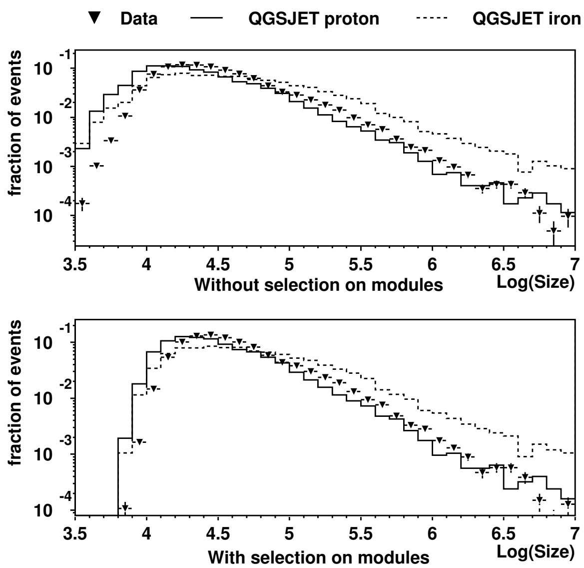

Figure 5.5: Shower size spectra, for data and proton simulations using QGSJET, without cut on the number of modules and with cut on the number of modules. Other models are similar. Distribution for iron showers shown for comparison.

The reason for this is the presence in the data of noise, which is not modeled in the detector response, in the form of displaced pedestals, as from time to time certain photomultipliers have for very short periods an increased dark current. This effect can be seen in figure 5.2.4 which shows for one day the readouts of the two photomultipliers connected to module 4. The left figure as on the abscissa the collected charge of the first photomultiplier, and on the ordinate the collected charge of the second photomultiplier, both pedestal subtracted. Next the main bulk of correlated readouts, one observes a second band starting at an ordinate of 47. The figure on the right shows the distributions for the single photomultipliers, whereas the first photomultiplier shows no problem, there is a small hint of the problem in the distribution obtained from the second photomultiplier, indicated by the arrow.

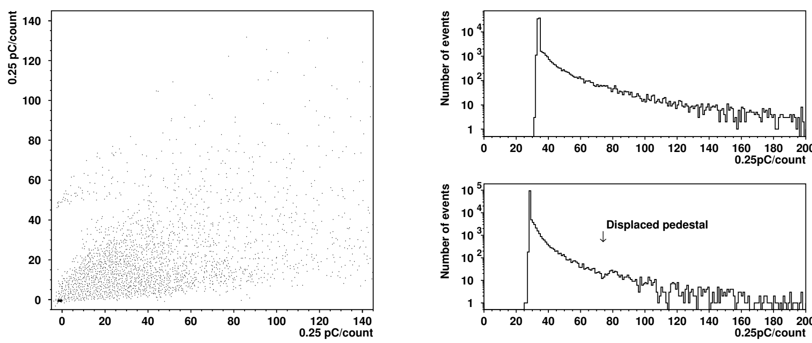

(a) distributions of the readouts of the second photomultiplier as function of the readout of the first photomultiplier

(b) The upper figure shows the distribution obtained from the first photomultiplier, in lower figure the distribution for the second photomultiplier

Figure 5.6: Distributions from the adc readouts for module 4, collected on one day.

To get this effect under control, we require that sufficient modules have readouts above one average MIP count. Figure 5.7 show the very good agreement, at least up to a number of modules hit of 42, of the distribution of number of modules hit for data and for the expectation for proton shower for the four interaction models. At high number of modules the unsimulated noise shows up in data. Also one has to notice the stability of the consistency of these distributions under the application of the different selections described in previous sections. When sufficient modules contribute to the fitting procedure, the influence of a single deficient readout gets under control. The selected events are those which have 20 or more modules with signal. This was a compromise as a selection of events with 30 or more modules would give perfect agreement but would severely cut in the statistics of small showers (with size below

$10^{4.5}$). It is also to notice that this selection only influences the smallest showers. The result of applying this selection is shown in the lower part of figure 5.7.

5.3 Fiducial phase space for muons in the Monte Carlo

In order to study the performances of the two muon counting methods, Mont Carlo is used. One has to compare the number of simulated muons in a well defined fiducial phase space, with the reconstructed number of muons. To minimise errors, this fiducial volume should be chosen as close to the detector as possible.

First a selection on the position of the muon is made. The CORSIKA simulation provides the muon positions on the roof of the SX-hall. A straight line extrapolation of their trajectory is made. If their distance of closest approach in the XY plane (bending plane) is less than 8 m and in the YZ plane (vertical plane passing through the beam pipe) less than 11 m, which has to be compared to the maximal size of the detector of 6.09 m and 8.08 m in the XY and YZ plane respectively, the muons are tracked through the detector simulation. This defines an effective surface of 352 m^2 which is independent of the muon direction.

Second a selection on the muon energy is applied. The molasse overburden imposes a sharp cut off at 17 GeV, yet the presents of the access shaft allows a small fraction of lower energetic muons to get through. Figure 5.8 show the muon distribution at the input of the detector simulation. Notice the small amount of muons below 2 GeV, they are muons produced within the overburden. The hatched area represents muons effectively reaching a virtual volume defined in the GEANT setup and closely encompassing the MUCH detector. Also the selection on the zenith angle has been applied here. In the rest of this work only muons with energy above 15 GeV will be considered. The fraction muons reaching the detector below this threshold represents 2.6 % (grey area in figure 5.8) and will be regarded as a systematic uncertainty. Also the implementation of the setup in GEANT is not accurate enough to fully describe the acceptance at the lowest energies.

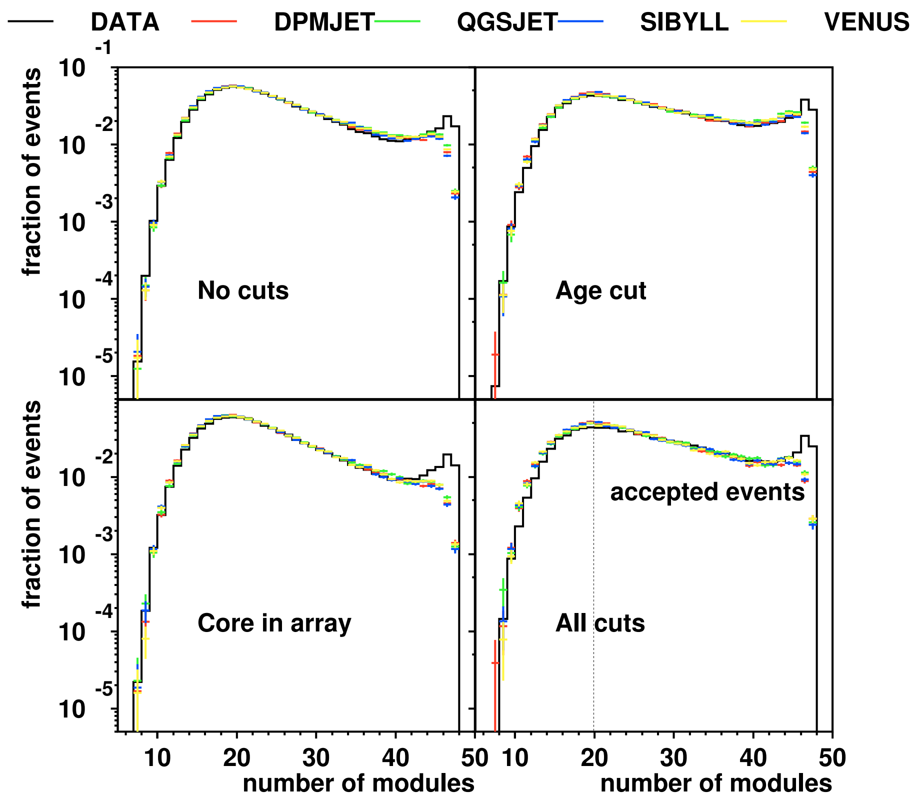

Figure 5.7: Distribution of the number of events, as function of the number of modules with signal they contain for data and MC. The upper left figure shows the distribution for all showers, in the upper right figure the age selection is applied, in the lower left figure the requirement on the shower core is applied, and both are applied in the lower right figure.

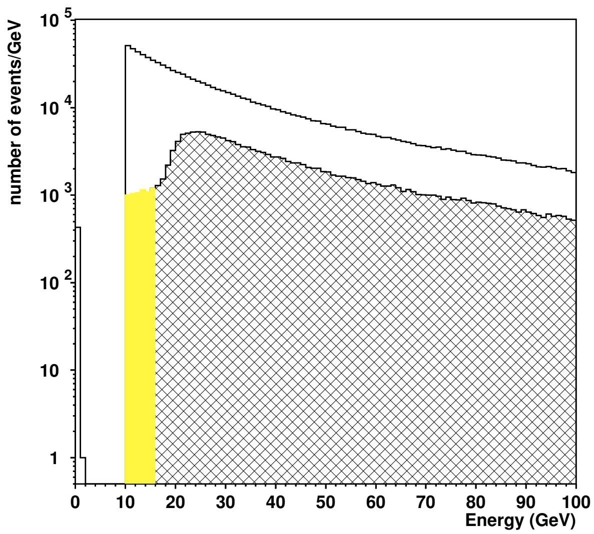

Figure 5.8: Simulated muons enrgy distribution. The hached area correspond to muons reaching the detector, within the selected zenith range. The grey area represent the low energy muons which reach the detector througth the shafts.

Chapter 6

Cosmic Ray composition and interaction models

"The Reason gives systems their structure, the data from experiments have to correspond exactly to the consequences of theory."

A. Einstein

6.1 Acceptance for proton showers

The acceptance of the Air Shower detector can be extracted from its Monte Carlo simulation, and will of course depend on the energy of the incoming particle, as well as its nature. Figure 6.1a shows the acceptance at the trigger level for proton induced showers. It increases constantly with energy as the lateral extent of the showers grow. Figure 6.1b shows the effective surface of the array for proton induced showers after application of the selections described in section 5.2. The effective area increases with energy up to 300 TeV and then stays constant at a value slightly higher than the surface defined in the selection. This is understood from the resolution at the boundary of the array allowing showers with core outside the array to be reconstructed inside.

Figures 6.1c and 6.1d shows the same quantities for iron induced showers. There is a noticeable difference in the shape of the raising part. As the iron-air cross-section is larger than the proton-air cross-section, iron induced showers start higher up in the atmosphere and at ground the showers are observed in a later stage of their development having lost more particles. A second effect is that iron induced interactions produce larger number of particles, therefore the total energy is shared over more particles, creating a larger, but less penetrating shower. Thus only above 1 PeV the effective surface becomes constant.

6.2 Relation between size and primary energy

As the acceptance depends on the nature as well as the energy of the incoming particle, so will the shower size. Figure 6.2 shows, for different models and two compositions, the primary energy of showers given the logarithm of the observed size. The error bars shown are the standard deviation of a Gaussian distribution fitted to the logarithmic primary energy distribution at a given shower size. They therefore illustrate the error on a single measurement. A linear dependence has been estimated between the quantities, which shows to be reasonable in the proton case, but for the iron case shows significant additional structure above sizes of 10^6.

Comparing proton and iron, it is clear that one needs a significantly higher energetic iron shower to generate a shower of similar size as a proton induced shower. Also the derived slope in the relation is significantly different. This means that determining the primary energy of a shower, one would need to know the nature of the primary particle, which on a event by event base is not feasible. Hence in the rest of the discussion we restrict ourselves to the shower size. Also, to establish a relation between theses two quantities, an assumption had to made on the primary distribution: here a spectral index of -2.7 was assumed for both proton and iron energy spectra. Comparing the different models no noticeable differences are observed.

At large sizes, the uncertainty on the energy, is about 0.5 unit in the 10 base logarithm (i.e. $\Delta E/E \approx 1.2$), for protons is due essentially to the large fluctuation in the height of the first interaction. The error is reduced in the iron case, where interactions take place at a better defined altitude. Also the very thin scintillation detectors used in the Air Shower array make them sensitive to fluctuations in the energy deposited by the traversing particles.

6.3 Cosmic Ray spectral index

As a check of consistency the spectral index of the shower size distribution was measured and found to be -2.42±0.02. For this measurement only showers with a size above 10^5 were used, to be in the region in which the spectrum follows a power law. The size spectrum is harder than the energy spectrum of Cosmic Ray. This is explained by the fluctuations introduced when convoluting from primary energy to shower size, combined with the steeply falling nature of this spectrum. To compare the measure spectral index, different proton spectra were simulated with energy spectral indices ranging from -2.9 to -2.5. This was performed by reweighting the Monte-Carlo events according to the energy at which they were generated. For each spectrum, the spectral index of the shower size distribution was extracted. This is shown in figure 6.3. For all models the region of energy spectral indices, resulting in size spectral indices compatible with the measured one, are compatible with the proton spectral index 2.78±.04 above a rigidity of 10 GV measured by the AMS collaboration (AMS Collaboration 2002). The agreement is specially good for QGSJET & VENUS, and the results are summarised in table 6.1.

Model	index
DPMJET	-2.64 ± 0.075
QGSJET	-2.76 ± 0.09
SIBYLL	-2.64 ± 0.075
VENUS	-2.81 ± 0.07

Table 6.1: Energy spectral index compatible with the observed size spectrum.

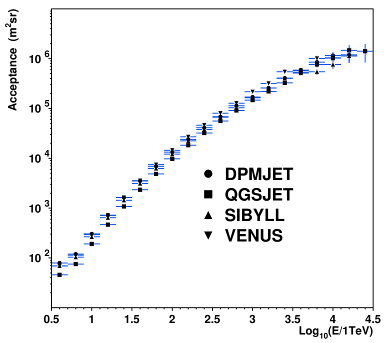

(a) Geometric acceptance a the trigger level, for proton showers, within a 60° cone around zenith, as function of primary energy.

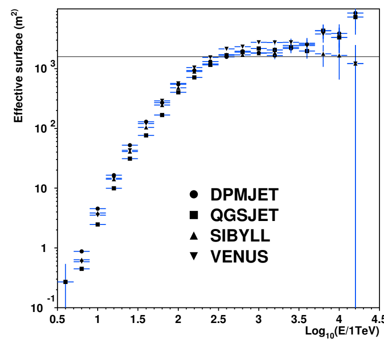

(b) Effective surface as function of primary energy for the selected proton showers, here the solid angle of the selection has been divided out.

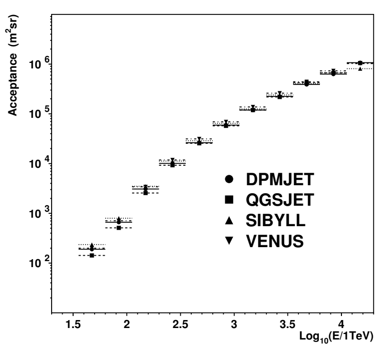

(c) Geometric acceptance a the trigger level, for iron showers, within a 60° cone around zenith, as function of primary energy.

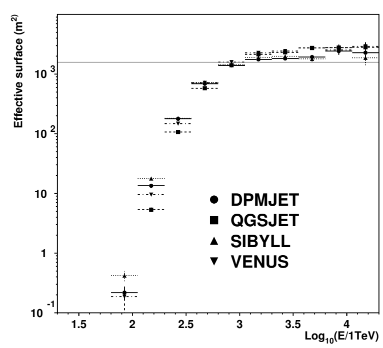

(d) Effective surface for the selected iron showers as function of primary energy, here the solid angle of the selection has been divided out.

Figure 6.1: Geometric quantities derived from Monte Carlo for proton and iron induced showers.

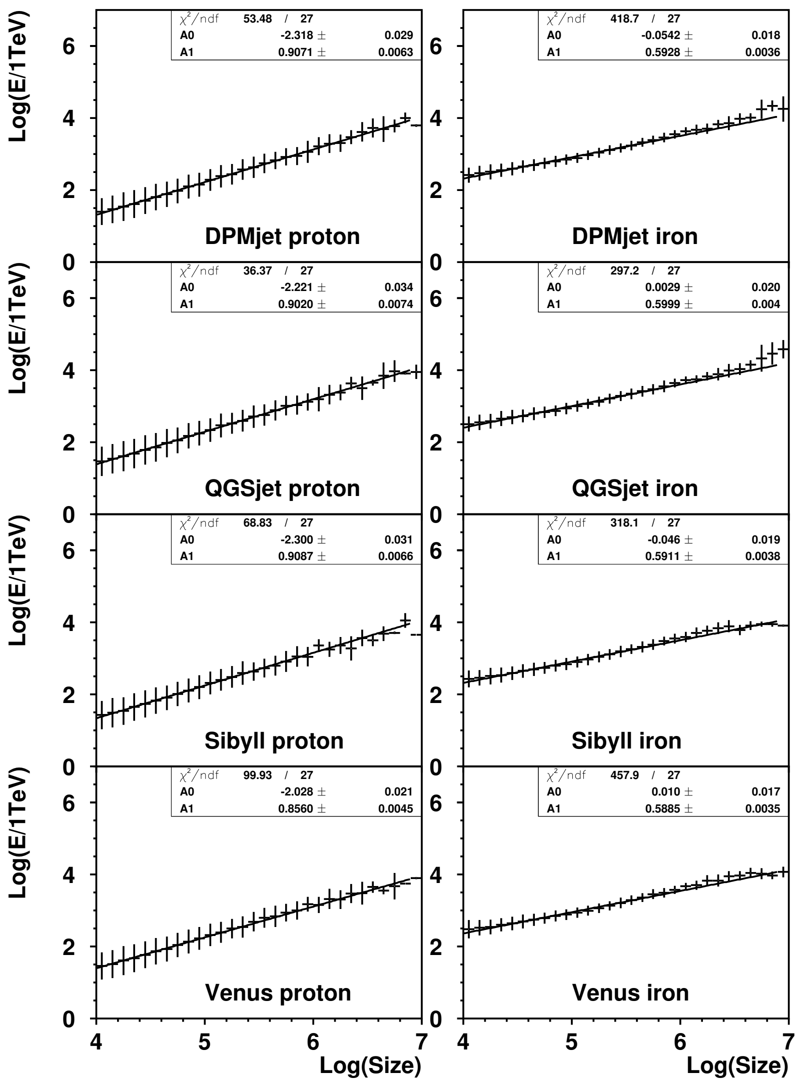

Figure 6.2: Relation between shower size and primary energy.

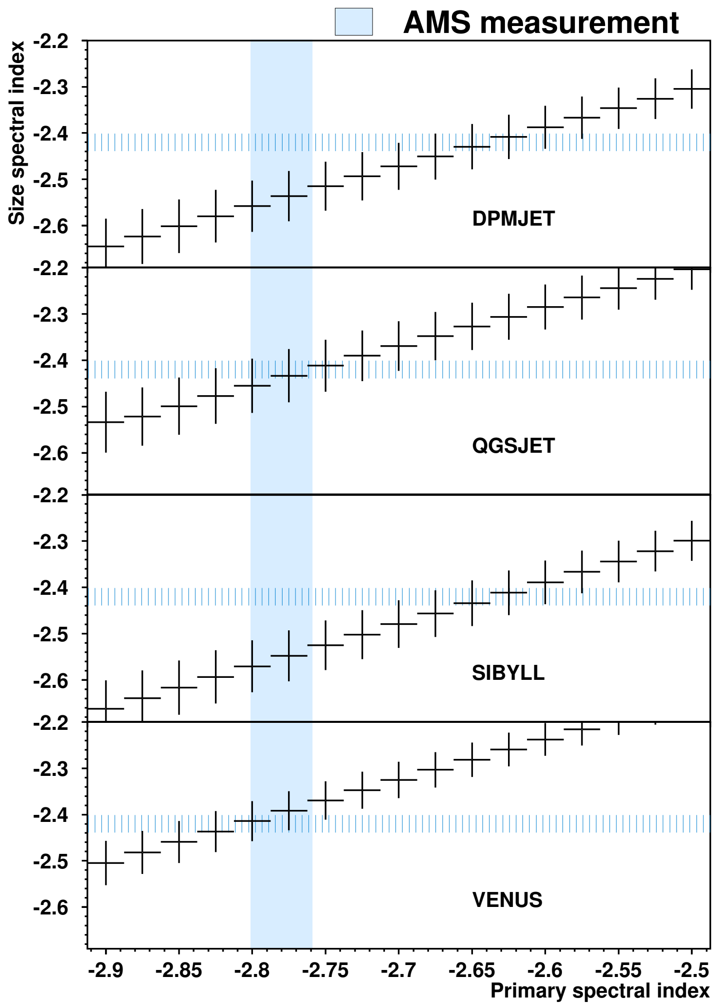

Figure 6.3: The spectral index of the shower size spectrum as function of the spectral index of the proton energy spectrum.

6.4 Muon counting

In this section the properties of the two muon counting algorithms will be assessed using the muons from the shower simulations, so that their energy distribution is close to reality. The fiducial surface in which muons are counted at the generator level has been described in section 5.3. This number of muons will be labelled n_μ^{MC}, the reconstructed number of muons with the CT algorithm will be n_μ^{CT}, and n_μ^{XO} the number of muons obtained from the XO algorithm. The capital N will be used to describe a number of events with given properties, for instance $N(n_\mu^{MC})$ will be the number of events generated counting n_μ^{MC} muons in the fiducial volume, and $N(n_\mu^{CT}|n_\mu^{MC})$ the number of events with a counted number of muons n_μ^{CT} knowing that n_μ^{MC} were present in the fiducial volume.

The most naive approach would be ti consider that each muon has a fixed probability p to be counted, independent of the presence of other muons. The distribution of events would then follow a binomial distribution:

$$N(n_\mu^{CT}|n_\mu^{MC}) = N(n_\mu^{MC})\mathcal{B}(p, n_\mu^{CT}, n_\mu^{MC}) \tag{6.1}$$

Where $\mathcal{B}(p, k, n)$ is the binomial probability of observing k out of n, with the single probability p. And similarly for the XO case.

This is in practise not the case, the probability of a muon to be counted decreases as more muons are around, as the counting algorithm gets more noise, and more complicated combinatorics to sort out. Therefore the probability p will be supposed to depend linearly to the number of muons in the fiducial volume:

$$p(n_\mu^{MC}) = p_0 + p_1 n_\mu^{MC} \tag{6.2}$$

Comparing this model to the data did not give completely satisfactory results. For low numbers of muons in the fiducial volume, a counted number of muons of 0 appears more often than expected. This fact can be modelled by introducing a global inefficiency. It will depend on the number of muons present and can be described by an exponential. The inefficiency:

$$\epsilon(n_\mu^{MC}) = p_2 \exp(-\frac{n_\mu^{MC}}{p_3}) \tag{6.3}$$

The number of events with counted number of muons n_μ^{CT}, with n_μ^{MC} muons present in the fiducial volume has now two cases:

$$N(n_\mu^{CT} = 0|n_\mu^{MC}) = N(n_\mu^{MC})\left(\epsilon(n_\mu^{MC}) + \left(1 - \epsilon(n_\mu^{MC})\right)\mathcal{B}(p, 0, n_\mu^{MC})\right) \tag{6.4}$$

$$N(n_\mu^{CT} > 0|n_\mu^{MC}) = N(n_\mu^{MC})\left(1 - \epsilon(n_\mu^{MC})\right)\mathcal{B}(p, n_\mu^{CT}, n_\mu^{MC}) \tag{6.5}$$

All the generated Monte-Carlo has been used to extract the four parameters for each of the counting methods. This is possible as the parametrisation is independent of the distribution of n_μ^{MC}. A likelihood minimisation was performed jointly on the 47 distributions from $n_\mu^{MC} = 2$ to $n_\mu^{MC} = 49$ and the result are shown in table:

method	p_0	p_1	p_2	p_3
XO	0.277 ± 0.001	-0.0010 ± 5.10^{-5}	0.98±0.03	3.86 ± .08
CT	0.247 ± 0.001	-0.0018 ± 5.10^{-5}	0.92±0.06	2.82 ± .10

Table 6.2: Results of the four parameters used to describe the performances of the muon counting.

Figures 6.4,6.5,6.6 & 6.7 compare the observed number of events in the Monte-Carlo for the 47 cases used in the fit, with the expectation from the fitted model, respectively for the CT counting and the XO counting. Whereas in the CT case, the model seem to give slightly broader distribution than observed in the simulations, a very good agreement is observed for the XO case.

From the model parameters, the XO counting results in a slightly higher number of muons than the CT method does (parameter p_0). Also the XO method is more steady, than the CT method, which is far less sophisticated suffers more trouble at high number of muons (parameter p_1). On the other side the CT method has a better efficiency at low number of muons (from parameter p_3), in agreement with the looser track definition for this algorithm.

To conclude, the two counting method give surprisingly similar results, and their results follow a simple and justified statistical model. However the inversion of the model has no known solution and will have to be done in a very heuristic fashion, as will be described later.

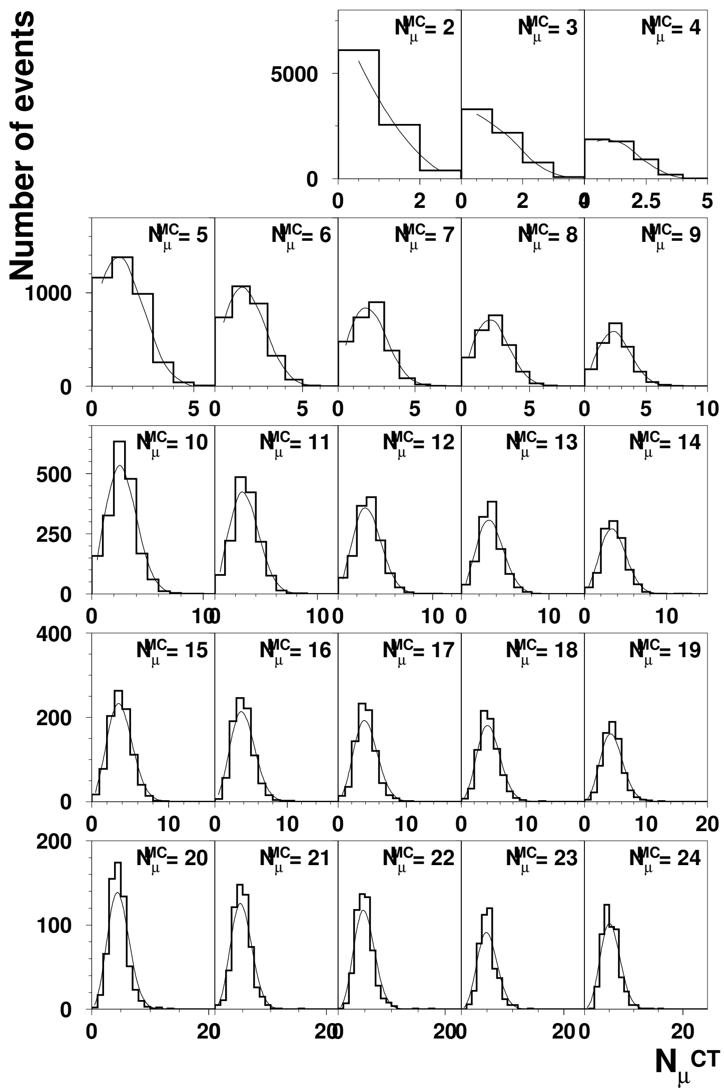

Figure 6.4: Distributions of $N(n_\mu^{CT}|n_\mu^{MC})$ used in the fit, compared to the fit result, the case n_μ^{MC} = 2 is displayed in the upper left, up to in the lower right the case n_μ^{MC} = 24.

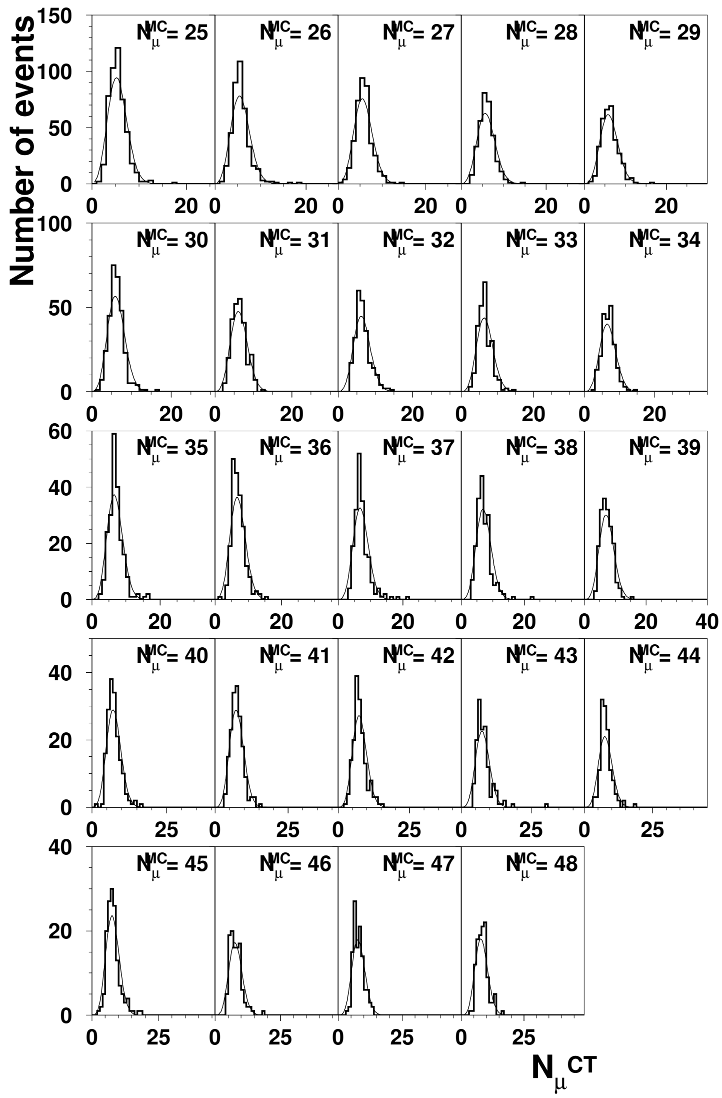

Figure 6.5: Distributions of $N(n_\mu^{CT}|n_\mu^{MC})$ used in the fit, compared to the fit result, the case n_μ^{MC} = 25 is displayed in the upper left, up to in the lower right the case n_μ^{MC} = 49.

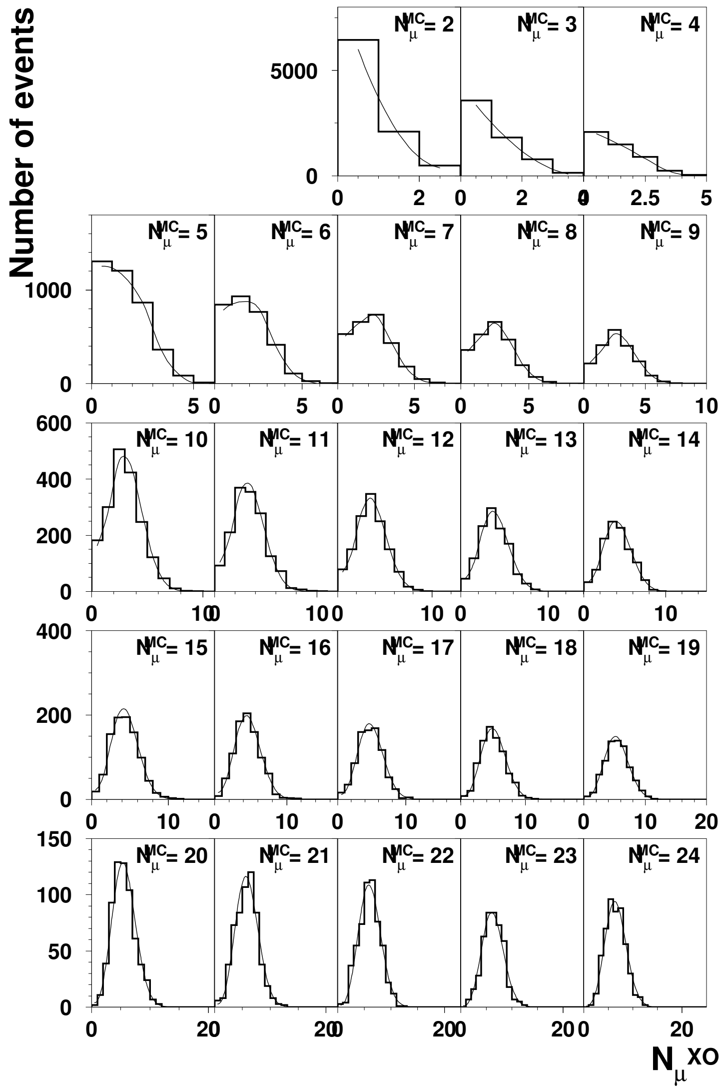

Figure 6.6: Distributions of $N(n_\mu^{XO}|n_\mu^{MC})$ used in the fit, compared to the fit result, the case n_μ^{MC} = 2 is displayed in the upper left, up to in the lower right the case n_μ^{MC} = 24.

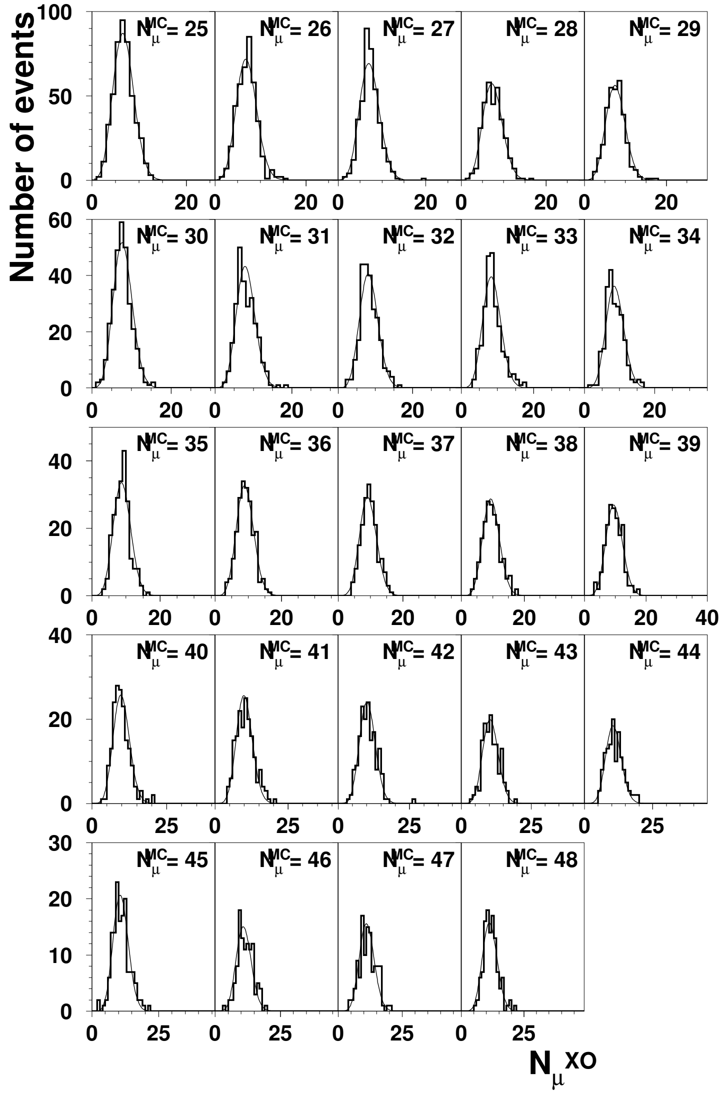

Figure 6.7: Distributions of $N(n_\mu^{XO}|n_\mu^{MC})$ used in the fit, compared to the fit result, the case n_μ^{MC} = 25 is displayed in the upper left, up to in the lower right the case n_μ^{MC} = 49.

6.5 Muon multiplicities as function of shower size

The original idea to extract the composition of Cosmic Ray in the energy range in which the array is sensitive was to perform a combined fit to the shower size and muon multiplicities, by reweighting the proton and iron Monte-Carlo distributions.

However observing figure 6.8 which compares the measured muon multiplicities in different shower size ranges with the predictions for proton and iron from the QGSJET model[1], suggest that there is little hope to get any sensitive result in this way. The muon numbers displayed in this figure were obtained with the CT counting method, and the number of entries have been normalised to the total amount selected events. The measured multiplicities agree almost perfectly with the iron simulations for all models, which would result composition, below the knee, dominated by heavy ions when the fit is performed. The main bulk of the measurements lays below 1 PeV (assuming proton primaries), and that in this range the composition has been established to be dominated by protons, as shown in figure 4, by several experiments. One then has to conclude that the problem lays in the prediction of high energy muons (i.e. with energy above 15 GeV) close to the core of the shower. The obtained result cannot be explained by an overestimation of the shower size in the simulations, as distributions obtained for proton simulations at high sizes do not describe the measured distributions at lower size.

It is thus not possible with current models of proton showers to correctly describe the abundance of high energy muons. As a consequences the admixture of heavy ions cannot be quantified.

It is to notice that the much higher number of muons appearing in nature, compared to what the models forecast has also been observed by the MACRO-EAS TOP combination (Macro and EAS-TOP Collaborations 1994) where the number of muons observed in data is even higher than those obtained for iron simulations in the two lowest shower size bins. Soudan-2 (Longley *et al.* 1995) also observes this, yet not as pronounced[2]. In the following, the multiplicity distributions are presented in terms of variables likely to be useful in improving the current models.

The large amount of events in data without muons is understood as inefficiencies present in the MUCH detector, are not simulated in the virtual detector used for the simulations. Also performing the same comparison of the muon numbers between data and the simulations, replacing for the simulations the selection on the reconstructed shower core position by a selection on the true shower core position, excludes the resolution as cause of the discrepancies.

[1]The other models are not shown here as they lead to very similar distributions.

[2]None of the publications comment on high muon abundance

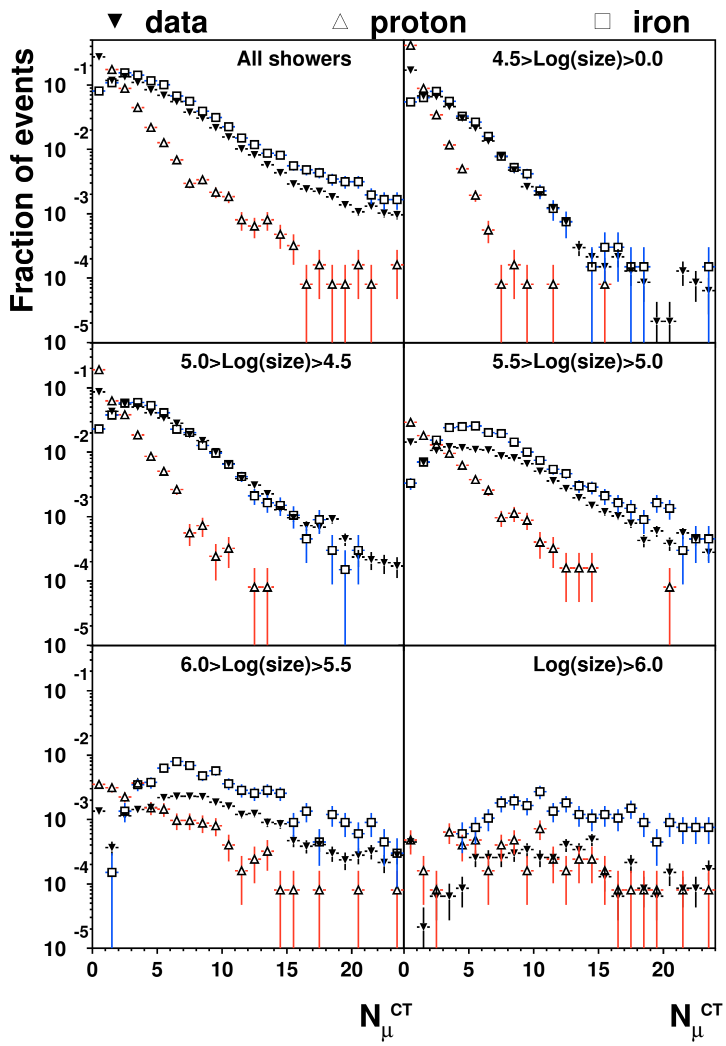

Figure 6.8: Comparison of the muon multiplicities obtained from the CT counting algorithm, between data, and the simulation results using the QGSJET model with proton and iron primaries, for all the showers, and in five different shower size ranges.

6.6 Muon multiplicities as function of pseudorapidity

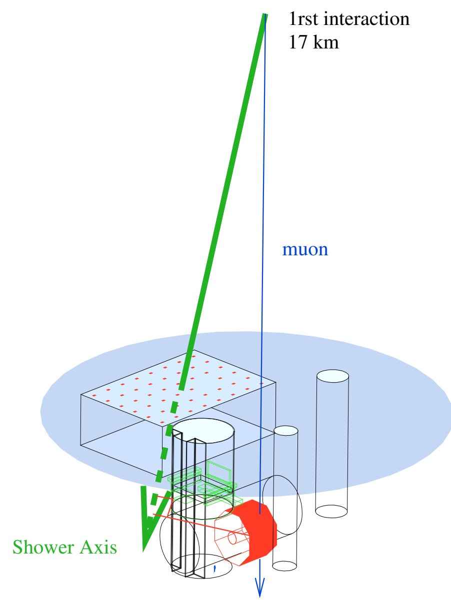

Figure 6.9: The L3+C setup as a forward particle production experiment.

Conceptually the L3+C setup acts as a fix target experiment in which particle production is probed, except for the size of the setup. Here the beam is the Cosmic Ray ray beam. The target is usually Nitrogen at the altitude of about 17 km (in the proton case) and a little higher for heavier elements. The position of the beam, and its energy is measured event by event, with the help of the Air Shower array. And there is a telescope, probing different regions at small angular distance from the beam, using the MUCH detector. This is schematically illustrated in figure 6.9

The possibility of measuring muon production at different angles from the shower core will be exploited in this section. The pseudorapidity η is a variable related to the angle θ at which a particle exits a reaction measured from the beam direction:

$$\eta = -\ln(\tan(\frac{\theta}{2})) \qquad (6.6)$$

The interest of the pseudorapidity is that for highly relativistic particles and at angle $\theta \gg 1/\gamma$ it can be assimilated to the rapidity y:

$$y = -\tanh^{-1}(\frac{p_z}{E}) \tag{6.7}$$

Where p_z is the particle momentum in the beam direction. The rapidity transforms under Lorentz boost as $y \rightarrow y - \tanh^{-1}(\beta)$.

In the case of the L3+C setup the pseudorapidity can be estimated using the height H of the first interaction, and the distance d between the shower axis and the centre of the MUCH detector. In the proton case the average $< H >= 17.5$ km can be used as an estimator of the single event height. It's r.m.s. of 8 km is the largest source of uncertainty on η. The distributions of the height of the first interaction for the four considered interaction model are shown in figure 6.10, their mean values agree with each other to better than 1 km. The distances d range from 0 to 90 m, with a resolution estimated from the Monte-Carlo of 3.5 m. The expression for the pseudorapidity is then:

$$\eta = -\ln(\tan(\frac{d}{2H})) \tag{6.8}$$

The average uncertainty on η is 0.4 units, mainly from the uncertainty on the primary interaction height. The pseudorapidity range covered starts at 6 for the showers for which the MUCH detector is the furthest away from the shower axis. It is limited at the higher end at 8.5 when the shower core passes through the MUCH detector.

The estimation of the average number of muons in each pseudorapidity bin is performed in the following way. From the counted number of muons, an estimation is made of the number of muons present in the fiducial surface defined in section 5.3. Ideally the counted number of muons should be unfolded, using for instance a Baysian method as described in (D'Agostini 1995). However two problems are faced: first a good estimate of the prior distribution is needed. Second the statistics in the extreme bins is too low and such methods fail.

A simple option is to use parameter p_0 described in section 6.4: $n_\mu^{MC} = n_\mu^{CT}/p_0$, or $n_\mu^{MC} = n_\mu^{XO}/p_0$ for the two counting methods respectively. This ignores parameter p_1, therefore at high counted number of muons the number of muons present in the fiducial volume would be underestimated in the case each value of n_μ^{MC} was equiprobable. Also the inefficiency, is not taken into account. One could have argued to assign $n_\mu^{MC} = p_2 p_3$ when no muons are counted. But this should be corrected for the probability of observing events with truly no muons in the fiducial volume. Again this depends on the prior distribution and not available. The choice was made, as no good prior is available, to ignore the effect of the inefficiency, also resulting in a underestimation of the number of muons. This is the only priorless estimator available.

The estimated number of muons is then multiplied by the ratio of the phase space of the pseudorapidity bin by the phase space of the fiducial surface to which the number of muons have been corrected. Finally the size of the pseudorapidity bin is divided out.

To make use of the two measurements available, their average was used, and the difference between the mean number of muons obtained from the two counting methods is used as a systematic error. The statistical error is extracted from the variance of the number of muons in each bin, and also the 3.5 % error from the 15 GeV cut on the muon energy is assigned as an error.

To summarise we now have a way to estimate the average number of muons above an energy threshold of 15 GeV, in each pseudorapidity bin, and this can be done as function shower size. Figure 6.11 shows the evolution of the average number of muons as function of pseudorapidity for different ranges of shower size.

Figures 6.12 to 6.15 show the results of such measurements for all showers combined and in five ranges of shower size, compared to all interaction model studied here. In the four lowest size regions the number of muons observed in the data is very close to the prediction for iron primaries, and that independently from the interaction model used. Only for shower in the highest shower size range, when the particle production in the central region of the interaction starts to contribute, the predictions for proton showers approaches the measurements.

When translating pseudorapidity to rapidity it must be kept in mind that the condition $\theta \gg 1/\gamma$ is certainly not satisfied for the muons of energy of order 20 GeV so that the relation $\eta \approx y$ does not hold. However one can estimate the shift in rapidity corresponding to the transformation from the laboratory frame to the centre of mass frame. Table 6.3 shows the rapidity shift assuming proton on Nitrogen reactions and different energies. As the shift depends to first order only on the ratio of the target to projectile momentum, and only to second order on the projectile mass to projectile momentum ratio, it depends little on the composition of the incoming particle.

Energy	10 TeV	100 TeV	1 PeV	10 Pev
Δy	3.63	4.78	5.93	7.09

Table 6.3: Rapidity shifts from laboratory frame to CM frame, for protons on Nitrogen.

Two other facts have to be kept in mind, when interpreting these distributions. A fraction of the muons originate from pion produced only in a later stage of the shower development and not in the first interaction. Also the scatterings during the propagation of the muons in the atmosphere add an additional resolution to the relation between production angle θ and the distance at which they are observed from the shower axis.

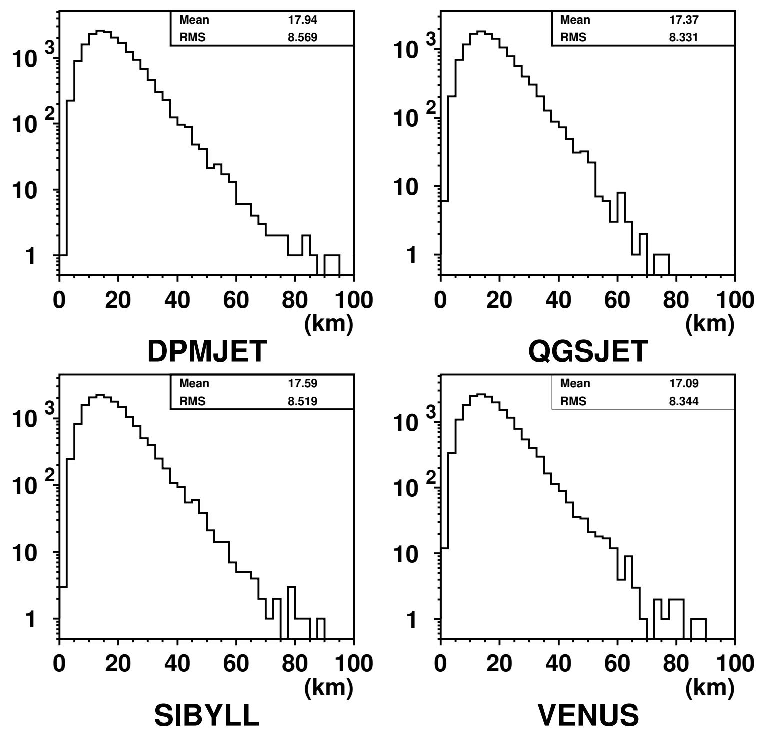

Figure 6.10: Distributions of the height of the first interaction for the four interaction models, the primary particles are protons.

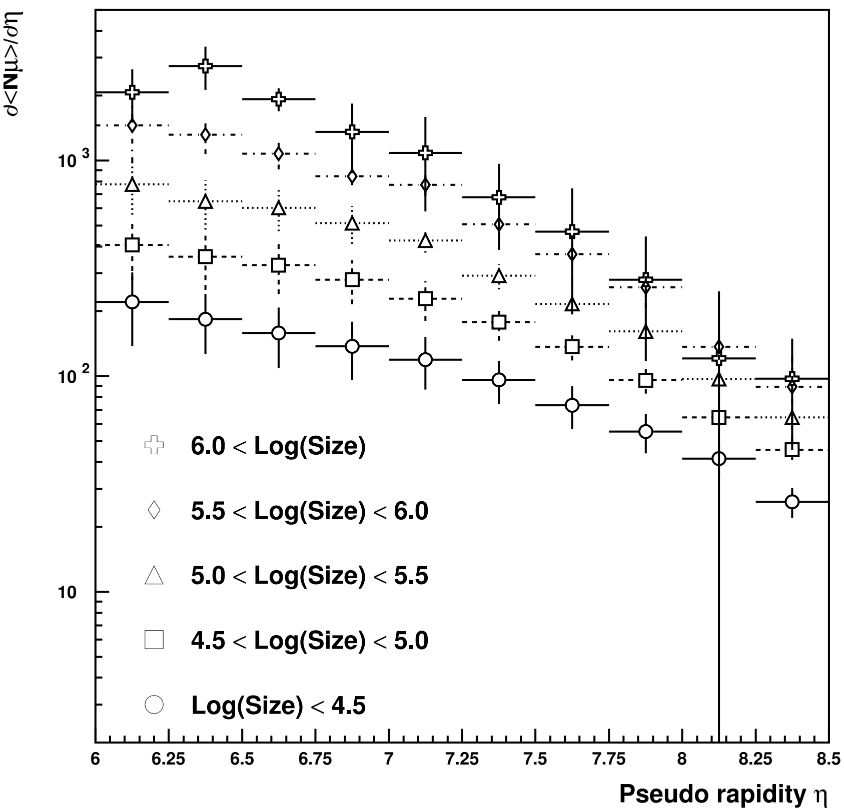

Figure 6.11: Average number of muons with energy above 15 GeV, per unit of pseudorapidity defined assuming an interaction at 17.5 km altitude, in five ranges in shower size.

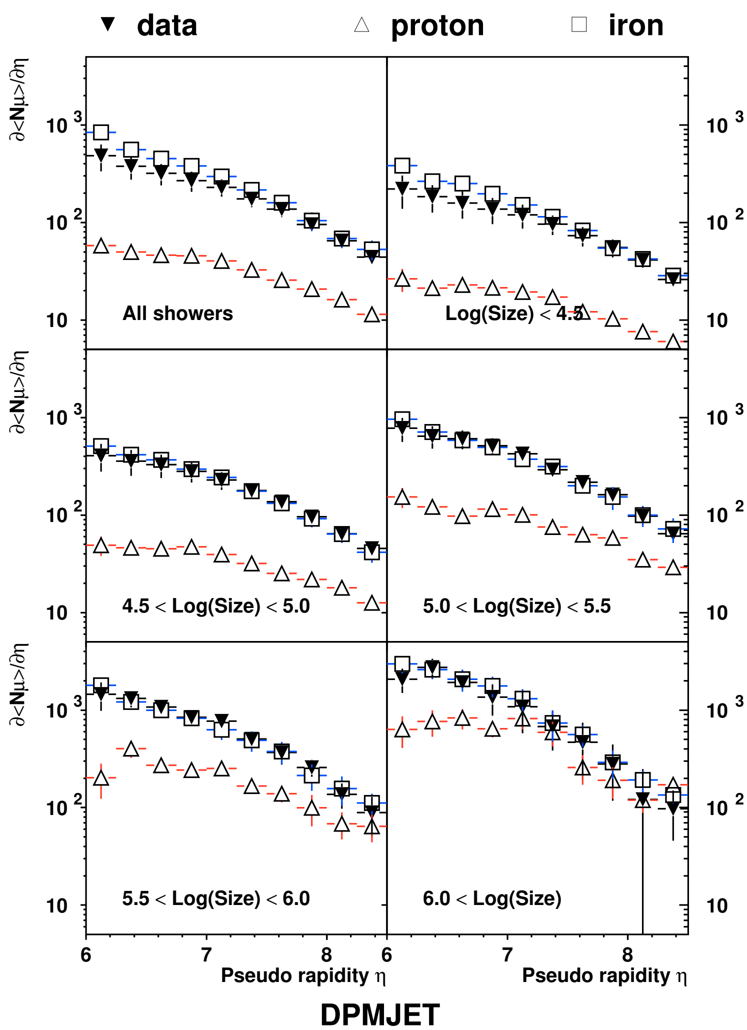

Figure 6.12: Average number of muons with energy above 15 GeV, per unit of pseudorapidity defined assuming a proton interaction at 17.5 km altitude. Result with DPMJET interaction model.

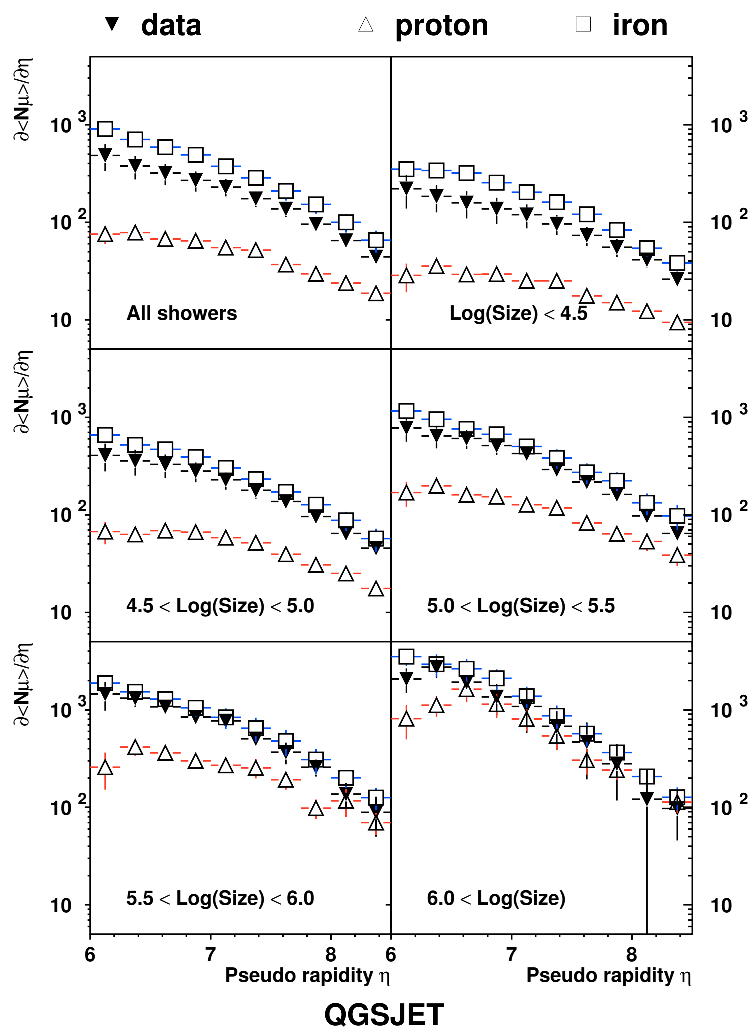

Figure 6.13: Average number of muons with energy above 15 GeV, per unit of pseudorapidity defined assuming a proton interaction at 17.5 km altitude. Result with QGSJET interaction model.

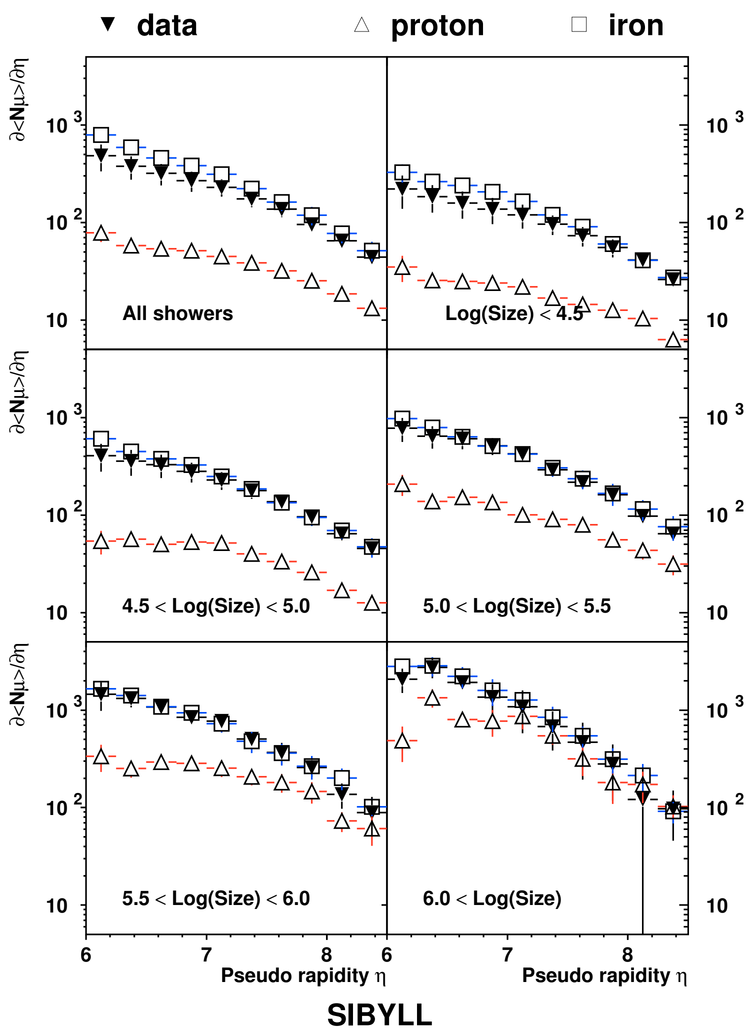

Figure 6.14: Average number of muons with energy above 15 GeV, per unit of pseudorapidity defined assuming a proton interaction at 17.5 km altitude. Result with SIBYLL interaction model.

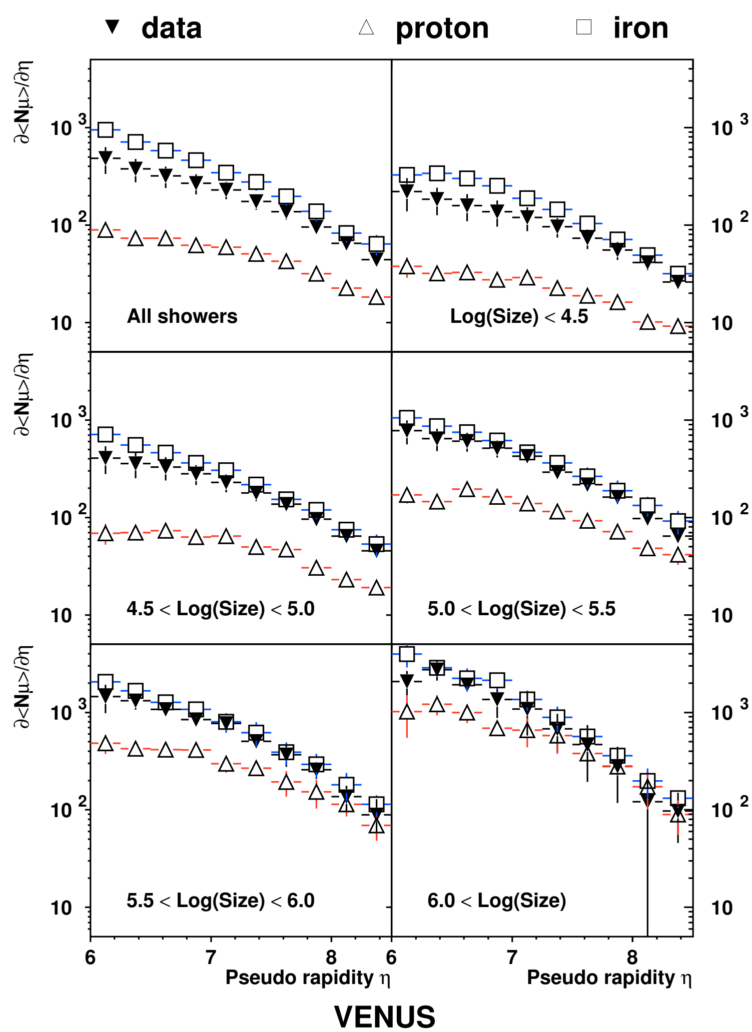

Figure 6.15: Average number of muons with energy above 15 GeV, per unit of pseudorapidity defined assuming a proton interaction at 17.5 km altitude. Result with VENUS interaction model.

6.7 Conclusions

Summarising the obtained results, the shape of the observed shower size distribution, from the Air Shower Array alone, agrees with known data. The multiplicity, and pseudorapidity distributions, for muons with energy above 15 GeV, have been measured as function of the Air Shower size, i.e. with the needed reserves as function of primary energy. The results when interpreted through the current interaction models, would indicate a dominance of heavy ions below the knee, in disagreement with direct measurements on top of, and above the atmosphere.

Current Air Shower models thus fall short of explaining the rather abundant muon production at high muon and modest primary energies. Data are presented as a function of variables likely to be relevant when searching for improvements of current models, namely pseudorapidity and energy.

Looking forward, the KASCADE setup has been extended with a muon detector, called muon tunnel, at a very shallow depth. The resulting threshold for muons is 0.8 GeV, which places this analysis in a completely different energy range than L_3+C, and both experiments nicely complement each other. The results presented in this work open a new window on the understanding of muon production in Air Shower, and thus pion production in the high energy nuclei interaction.

Unfortunately the large computing resources needed by the complete simulation of Air Shower, has limited this work in the following ways: First only one transport code has been studied, namely CORSIKA, which does not allow to exclude a possible loss of muon in the transport code. Second the most recent and promising interaction model NeXuS could not be tested. And Finally the replacement GEISHA, for the low energy nuclear interactions, by URQMD had also to be excluded in light of the required computing resources.

More data from accelerators will soon allow a better constraint of the interaction models. This data is being collected using the CDF (Cihangir, Marchetto, McIntyre, Meyer & Webb 1988) detector at the TEVATRON accelerator. In a more distant future relevant data will also be collected at the LHC collider, especially by the TOTEM collaboration (TOTEM Collaboration 1999). These measurements, together with data obtained from Cosmic Ray experiments, will allow progress on the quality of the interaction models, and hopefully consensus will be reached as to the behaviour of the Cosmic Ray composition, thus allowing for astrophysical interpretations.

List of Figures

Bibliography

Achterberg, A. (1997). “Cosmic ray physics, sources of energetic particles in the universe”. Lecture notes, University of Utrecht.

Alfvén, H., “On the existance of electromagnetic hydrodynamic waves”. *Ark. Astron. Fys.* **29B**(1943):p. 1.

AMANDA Collaboration, “The AMANDA neutrino telescope: principle of operation and first results”. *Astropart. Phys.* **13**(2000):pp. 1–20.

AMS Collaboration, “Antimatter spectrometer in space”. *Nucl. Instr. and Meth.* **A350**(1994):pp. 351–367.

AMS Collaboration, “Cosmic protons”. *Phys. Lett.* **B490**(2000a):pp. 27–35.

AMS Collaboration, “Helium in near earth orbit”. *Phys. Lett.* **B494**(2000b):pp. 193–202.

AMS Collaboration, “The alpha magnetic spectrometer (ams) on the internal space station: Part i - results from the test flight on the space shuttle”. *Phys. Rep.* **366**(2002):pp. 331–405.

Anderson, C. D., “The positive electron”. *Phys. Rev.* **43**(1933):pp. 491–494. Positron discovery.

ANTARES Collaboration, “The antares optical module”. *Nucl. Instr. and Meth.* **A484**(2002):pp. 369–383.

Auger, P. & Maze, R., “Extension et pouvoir penetrant des grandes gerbes de rayons cosmiques”. *C. R. Acad. Sci. (Institut de France)* **208**(1939):p. 164.

Bagduev, R. I. *et al.*, “The optical module of the baikal deep underwater neutrino telescope”. *Nucl. Instr. and Meth.* **A420**(1999):pp. 138–154.

Bähr, J. *et al.* (1996). *Precision measurement of the cosmic ray muon momentum spectrum between 20 and 2000 GeV/c* . CERN. L_3 internal note 1977.

Bähr, J. *et al.*, "An effective method to read out large scintillator areas with precise timing". In "SCIFI97: Conference on Scintillating and Fiber Detectors", (1997), pp. 385–392.

Balkanov *et al.*, "Baikal experiemtn status report". In "Nuc. Phys.", (2002), vol. B110, pp. 504–506.

Bass, S. A. *et al.*, "Microscopic models for ultrarelativistic heavy ion collisions". *Prog. Part. Nucl. Phys.* **41**(1998):pp. 225–370.

Bell, A. R., "The accelaeration of cosmic rays in shick fronts-i". *Mon. Not. R. ast. Soc.* **182**(1978):pp. 147–156.

Bleicher, M. *et al.*, "Relativistic hadron-hadron collisions in the ultra-relativistic quantum molecular dynamics model". *J. Phys. G* **25**(1999):pp. 1859–1896.

Borione, A. *et al.*, "A large air shower array to search for astrophysical sources emitting γ-rays with energies greater-than or equal to 10^{14} ev,". *Nucl. Instr. and Meth.* **A 346**(1994):pp. 329–352.

Brouwer, C. *et al.*, "The magnetic measurement system of the L_3 detector". *Nucl. Instr. and Meth.* **A313**(1992):pp. 50–62.

Brun, R. *et al.* (1994). *GEANT, Detector description and simulation tool*. CERN, Geneva.

Capdevielle, J. N. *et al.*, "Lateral distributions, localization methods, $\rho(600)$, size and energy determination in giant eas". In "Nucl. Phys.", (2001), vol. B97, pp. 223–226.

Christiansen, J. (1997). *32 Channel general purpose Time to Digital Converter*. CERN/ECP-MIC.

Cihangir, S., Marchetto, F., McIntyre, P., Meyer, T. & Webb, R., "The cdf forward / backward hadron calorimeter." *Nucl. Instr. and Meth.* **A267**(1988):p. 249.

Clay, J., "Penetrating radiation". *Proc. R. Acad. Amsterdam* **31**(1928):p. 1091.

Compton, A. H., "Variation of the cosmic rays with latitude". *Phys. Rev.* **41**(1932):pp. 111–113.

Compton, A. H., "A geographic study of cosmic rays". *Phys. Rev.* **43**(1933):pp. 387–403.

D'Agostini, G., "A multidimentional unfolding method based on bayes' theorem". *Nucl. Instr. and Meth.* **A362**(1995):pp. 487–498.

Drescher, H. J., Haldik, M., Ostapchenko, S., Pierog, T. & Werner, K., "Parton-based Gribov-Regge theory". *Phys. Rep.* **350**(2001):pp. 93–289.

Fermi, E., "On the origin of the cosmic radiation". *Phys. Rev.* **75**(1949):pp. 1169–1174.

Fletcher, R. S., Gaisser, T. K., Lipari, P. & Stanev, T., "SIBYLL: an event generator for simulation of high energy cosmic ray cascade". *Phys. Rev.* **D50**(1994):pp. 5710–5731.

Fukuda, Y. *et al.*, "Evidence for oscillation of atmospheric neutrinos". *Phys. Rev. Lett.* **81**(1998):pp. 1562–1567.

Ginzburg, V. L. & Syrovatskii, S. I., *The origin of Cosmic rays* (Pergamon press, 1964).

Greisen, K., "Cosmic ray showers". *Annu. Rev. Nucl. Sci.* **10**(1960).

Greisen, K., "End of the cosmic-ray spectrum?" *Phys. Rev. Lett.* **16**(1966):pp. 748–750.

Gribov, L. V., Levin, E. M. & Ryskin, M. G., "Semihard processes in QCD". *Phys. Rep.* **100**(1983):pp. 1–150.

Grigorov, N. L. *et al.*, "Energy spectrum of cosmic ray α-particles in $5{\times}10^{10}$-10^{12} eV/nucleon energy range". In "Proceedings 12th International Cosmic Ray Conference", (edited by Hobart) (1971), vol. 5, pp. 1760–1766. Proton Satellite.

Groenstege, H. L., Rewiersma, P. A. M., Wijnen, T. A. M. & Zwart, A. N. M. (1999a). *The NIMROD, 16 channel read out driver used in the L3 +Cosmic project*. NIKHEF. ETR 99-06.

Groenstege, H. L., Wijnen, T. A. M., Rewiersma, P. A. M. & Stolte, J. (1999b). *Cosmic Personality Card for the L3 +Cosmics experiment*. NIKHEF. ETR 99-02.

Hagiwara, K. *et al.*, "Review of Particle Physics". *Phys. Rev.* **D66**(2002):pp. 010001+. *http://pdg.lbl.gov

Halzen, F. *et al.*, “From the first neutrino teloscope, the Anartic Muon and Neutrino Detector Array AMANDA, to the icecube observatory”. In “Proceedings of the 26th International Cosmic Ray Conference”, (edited by Kieda, D., Salamon, M. & Dingus, B.) (Salt lake City, 1999), vol. 2, pp. 428–431.

Hayakawa, S., *Cosmic Ray physics*, vol. XXII of *Interscience monographs and texts in physics and astronomy* (Jhon Wiley & Sons, 1969).

Heck, D. & Knapp, J. (2001). *Extensive air shower simulation with CORSIKA: A user’s guide*. Karlsruhe.

Heck, D., Knapp, J., Capdevielle, J., Schatz, G. & Thouw, T. (1998). “CORSIKA: A monte-carlo code to simulate extensive air showers”. Tech. rep., Forschungszentrum Karlsruhe.

HEGRA Collaboration, “The time structure of Čerenkov images generated by TeV γ-rays and by cosmic rays”. *Astropart. Phys.* **11**(1999):pp. 363–377.

Hess, V. F., “Über Beobachtungen der durchdringenden Strahlung bei sieben Freiballonfahrten”. *Phys. Z.* **13**(1912):pp. 1084–1091.

Hinton, J. A. (1998). *Ph.D. Thesis*. Ph.D. thesis, Univ. of Leeds.

Hörandel, J., “On the knee in the energy spectrum of cosmic rays”. In “Proceedings of the 27th International Cosmic Ray Conference”, (Copernicus Gesellschaft, Hamburg, 2001), pp. 71–74.

Hughes, E. *et al. IEEE Trans. Nucl. Sci.* **NS-27**(1980):p. 364.

JACEE Collaboration, “Cosmic-ray proton and helium spectra: Results from the jacee experiment”. *ApJ.* **502**(1998):pp. 278–283.

James, F. (1994). *MINUIT Function Minimization and Error Analysis*. CERN, Geneva, Zwitserland.

Kalmykov, N. N., Ostapchenko, S. S. & Pavlov, A. I., “Quark-gluon-string model and eas simulation problems at ultra-high energies”. In “Nucl. Phys.”, (1997), vol. B52, pp. 17–28.

Kamata, K. & Nishimura, J. *Suppl. Prog. Theor. Phys.* **6**(1958).

Karimäki, V., “Effective circle fitting for particle trajectories”. *Nucl. Instr. and Meth.* **A305**(1991):p. 187.

Kasahara, S. M. *et al.*, “A study of cosmic ray composition in the knee region using multiple muon events in the soudan 2 detector”. *Phys. Rev.* **D55**(1997):pp. 5282–5294.

KASCADE Collaboration, “The detedtor system for measurement of multiple cosmic muons in the central detector of kascade”. *Nucl. Instr. and Meth.* **A465**(2001a):pp. 455–471.

KASCADE Collaboration, “Electron, muon, and hadron lateral distributions measured in air showers by the kascade experiment”. *Astropart. Phys.* **14**(2001b):pp. 245–260.

KASCADE Collaboration, “Time structure of extesive air shower muon component measured by the kascade experiment”. *Astropart. Phys.* **15**(2001c):pp. 149–165.

Kirk, J. G., *Plasma Astrophysics*. No. 24 in Saas-Fee Advanced Course (Springer-Verlag, 1994).

Kolhörster, W., Matthes, J. & Weber, E. *Naturwiss* **26**(1938):p. 576.

L3 Collaboration, “The construction of the L3 experiment”. *Nucl. Instr. and Meth.* **A289**(1990):pp. 35–102.

L3 F/B Muon Group, “The forward muon detector of L3”. *Nucl. Instr. and Meth.* **A383**(1996):pp. 342–366.

Lagutin, A. A., Plyasheshnikov, A. V. & Goncharov, A. I., “The lateral distribution of the electrons in the electromagnetic air shower”. In “Nucl. Phys.”, (1998), vol. B60, pp. 161–167.

Leich, H. (1998). *The GPSTIM: User’s Guide*. DESY-Zeuthen. 97?

Leijtens, X. J. M. (1993). *Production of tau pairs at the Z resonance*. Ph.D. thesis, University of Amsterdam.

Linsley, J., “Evidence for a cosmic ray particle with energy 10^{20} ev”. *Phys. Rev. Lett.* **10**(1963):pp. 146–148.

Longair, M. S., *High energy astrophysics* (Cambridge University Press, 1981).

Longley, N. P. *et al.*, “Ultrahigh energy cosmic ray composition from surface air shower and underground muonmeasurements as soudan-2”. *Phys. Rev.* **D52**(1995):pp. 2760–2765.

LVD and EAS-TOP Collaborations, "The high energy muon spectrum in extensive air showers: fist data from LVD eand EAS-TOP at Gran Sasso". *AstroPP* **9**(1998):pp. 185–192.

Macro and EAS-TOP Collaborations, "Study of the primary cosmic ray composition around the knee of the energy spectrum". *Phys. Lett.* **B 337**(1994):pp. 376–382.

Micono, M., Zurlo, N., Massaglia, S., Ferrari, A. & Melrose, D. B., "Diffusive shock acceleration in extragalactic jets". *Astron. Astrophys.* **349**(1999):pp. 323–333.

MILAGRO Collaboration, "A survey of the northern sky for tev point sources". *AstroPJ* **558**(2001):pp. 477–481.

Neddermeyer, S. H. & Anderson, C. D., "Note on the nature of cosmic ray particles". *PhysRev* **51**(1937):pp. 884–886. Muon discovery.

Nelson, W. R., Hirayama, H. & Rogers, D. W. O. (1985). "The EGS4 code system". Tech. Rep. SLAC-265, Stanford Linear Accelerator Center.

NESTOR Collaboration, "NESTOR neutrino telescope status report". In "Nucl. Phys.", (edited by Dobrigkeit, C. & Rigitano, R.) (2001), vol. B97, pp. 105–198.

Ostapchenko, S., Thouw, T. & Werner, K., "The new venus model of hadronic interactions at ultrarelativistic energies". In "Nucl. Phys.", (1997), vol. B52, pp. 3–7.

Petersen, B. G. (2002). *The cosmic ray induced muon spectrum measured with the* L_3 *detector*. Ph.D. thesis, KUN.

Ranft, J., "Dual parton model at cosmic ray energies". *Phys. Rev.* **D51**(1995):pp. 64–84.

Rochester, G. D. & Butler, C. C., "Evidence for the existnce of new unstable elementary particles". *Nature* **160**(1947):pp. 855–857. Discovery Kaons.

RUNJOB Collaboration, "Composition and energy spectra of cosmic-ray primaries in the energy range 10^{13}-10^{15} eV/particle observed by Japanese-Russian joint balloon experiment". *Astropart. Phys.* **16**(2001):pp. 13–46.

Sangjin, L., Angela, O. V. & Guenter, S., "Extragalactic magnetic field and the highest energy cosmic rays". *ApJ.* **455**(1995):p. L21.

Schmitt, V. (2000). *Analysis of Multi Muon Events in the* L_3 *detector*. Master's thesis, Humboldt-University, Berlin.

Stozhkov, Y., Okhlopkov, V. & Pokrevsky, P., “Cosmic rays tell us on supernova explosion in the nearby interstellar space”. In “Nuc. Phys.”, (2001), vol. B97 of *Proc. Suppl.*, pp. 207–210.

Swordy, S. P. *et al.*, “The composition of cosmic rays at the knee”. *Astropart. Phys.* (2002). (to be published, astro-ph/0202159).

Timmermans, C. (1992). *Measurement of muon pair production around the Z-resonance uing the* L_3 *detector at LEP*. Ph.D. thesis, University of Nijmegen.

Timmermans, C. (2001). “Analysis possibilities on raw data”. L_3+C Note.

TOTEM Collaboration (1999). “Totem, total cross section, elastic scattering and diffraction dissociation at the lhc : Technical proposal”. Tech. Rep. CERN-LHCC-99-007 ; LHCC-P-5, CERN, Geneva.

Tuning, N. (2001). *Proton structure functions at HERA*. Ph.D. thesis, University of Amsterdam.

Verkooijen, H. (1999). *CTT-V2*. NIKHEF. ETR 99-01.

Zatsepin, G. T. & Kuzmin, V. A., “Upper limit of the spectrum of cosmic rays”. *JETP Lett.* **4**(1966):pp. 78–80.

Summary

The L3+C detector was used to measure muons from Cosmic Rays shortly in 1998, then from spring to autumn 1999 and in 2000. For the last period the setup was extended with a scintillator based Air Shower detector. The data collected that last year, during the periods of coincident running of the muon and Air Shower detector have been analysed and the results obtained are presented in this work.

Initially, the idea was to use the muon content of Air Showers in order to constrain the Cosmic Ray composition in the energy region directly below the knee. However comparison of the obtained muon densities with predictions for light (proton) and heavy nuclei (iron) obtained with different interaction models used in the Cosmic Ray community to describe the strong interaction show large discrepancies with expectation.

The setup allows for the first time to study the distribution of high energy muons (above 15 GeV) with Air Showers in the energy range 100 TeV to 10 PeV. The muon distributions have been presented in a detector independent way, and show that the number of muons predicted with all used interaction models used (DPMJET, QGSJET, SIBYLL & VENUS) underestimate the number of high energy muons in the core of the shower, especially at the lower energies.

As all methods to determine the Cosmic Ray composition in the knee region rely on these models, (with exception of direct measurements). This proves that further improvement in the interaction models, as well as more measurements of the particle production in the forward region are needed to reach an understanding of Cosmic Rays in the knee region and above.

Samenvatting

Gedurende een korte periode in 1998, en vervolgens van voorjaar tot najaar 1999 en 2000 werd de L3+C detector gebruikt voor het meten van muonen uit kosmische straling. Gedurende de laatste periode was de opstelling uitgebreid met een uit scintillator bestaande deeltjeslawine detector. De gegevens van deze deeltjeslawine en ondergrondse muon detector zijn gecombineerd en geanalyseerd. Deze combinatie van gegevens staat beschreven in dit werk.

Voordat de resultaten beschikbaar waren, was de opzet om het muon deel van de deeltjeslawine te gebruiken om de compositie van de kosmische straling te bepalen in het energie gebied juist onder de zogenaamde knie van het kosmische spectrum. De vergelijking van de gemeten muon dichtheid met de voorspellingen, waarbij gebruik is gemaakt van verschillende modellen voor de sterke wisselwerking, en waarbij zowel lichte (protonen) als zware (ijzerkernen) straling is gesimuleerd, toont aan dat er grote verschillen zijn tussen de data en verwachting.

De gebruikte opstelling gaf de mogelijkheid om, voor het eerst, de verdeling van hoog energetische muonen (boven 15 GeV) als functie van de grootte van de deeltjeslawine, in het energiegebied van 100 TeV tot 10 PeV, te bestuderen. In dit werk wordt de muon verdeling gepresenteerd op een manier waardoor de afhankelijkheid van de detector minimaal is. Dit geeft direct aan dat de aantallen hoog energetische muonen, zoals door de verschillende interactie modellen (DPMJET, QGSJET, SIBYLL en VENUS) wordt verspeld, in de kern van de lawine een onderschatting is, met name bij lage energieën.

Alle methoden die gebruikt worden om de compositie van kosmische straling te bepalen (met uitzondering van directe metingen), maken gebruik van deze modellen. Het is duidelijk dat een verbetering van de modellen, wat gepaard moet gaan met betere metingen in de voorwaartse richting, nodig is voor een beter begrip van de kosmische straling in het gebied van de knie, en ver hierboven.

Curriculum vitae

The author of this book was born on June 12 of 1973 in Crest (France). He passed his baccalauréat with mention in 1991 at the Lycée St. Victor in Valence. He then followed the Mathématique Supérieure and Mathématique Spéciale (M) classes at the Lycée Camille Vernet in Valence. Participating to the Concours Commun Polytechnique, the Concours Ecoles Normales Supérieur, and Ecoles Centrales, he chose to go to the Ecole Nationale Supériure de Physique de Marseille, till 1997. Parallel to his last year at the ENSPM, he attended the DEA Physique des particules, physique mathématique et modélisation at the Université du Var Toulon.

As an Erasmus student, he worked on the L_3+C experiment at the HEF department of the Katholieke Universiteit Nijmegen. This work granted him an diplôme d'ingénieur at the ENSPM, and the mention bien at the DEA graduation.

He got an Onderzoeker in Opleiding position at the KUN, in september 97, to continue working on the L_3+C experiment. He was detached for 22 month at CERN to actively participate in the building of the experiment as well as the development of the associated software. In febuary 2000 he returned to Nijmegen to finish his doctoral work. The author presented the L_3+C experiment and its results at the First Artic Workshop (Sodankÿla 1999), at the XIth International Symposium on Very High Energy Cosmic Ray Interaction (Campinas 2000), assisted the Chacaltaya Meeting (La Paz 2000), presented his results at the 27th International Cosmic Ray Conference (Hamburg 2001), a the 18th European Cosmic Ray Symposium (Moscow 2002), and at the XIIth International Symposium on Very High Energy Cosmic Ray Interaction (Geneva 2002).